J. Fluid Mech. (2022), *vol*. 938, A36, doi:10.1017/jfm.2022.184

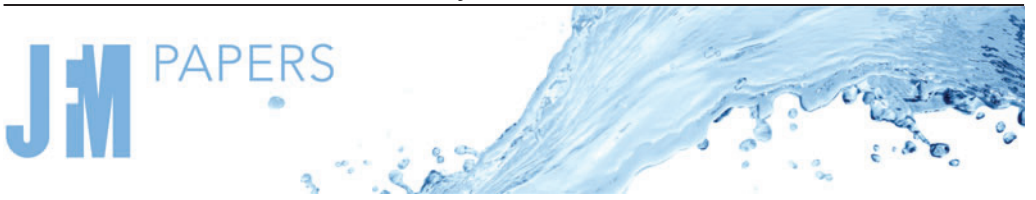

Transient wave-induced pore-water-pressure and soil responses in a shallow unsaturated poroelastic seabed

Linlong Tong[1,2,3] **and Philip L.-F. Liu**[2,4,5,6,†]

[1]Key Laboratory of Ministry of Education for Coastal Disaster and Protection, Hohai University, Nanjing 210098, PR China

[2]Department of Civil and Environmental Engineering, National University of Singapore, 117576, Republic of Singapore

[3]College of Harbor, Coastal and Offshore Engineering, Hohai University, Nanjing 210098, PR China

[4]Institute of Hydrological and Oceanic Sciences, National Central University, Jhongli, Taoyuan 320, Taiwan, ROC

[5]School of Civil and Environmental Engineering, Cornell University, Ithaca, NY 14850, USA

[6]Department of Hydraulic and Ocean Engineering, National Cheng Kung University, Tainan, 10701 Taiwan, ROC

(Received 5 July 2021; revised 16 December 2021; accepted 22 February 2022)

An analytical solution is developed for studying transient water wave-induced responses inside an unsaturated poroelastic seabed of finite thickness. The soil skeleton and the pore fluid are compressible and the constitutive relationship of the soil skeleton is described by Hooke's law. Assuming that the horizontal length scale of wave motion is much larger than the seabed thickness, the leading-order analytical solutions for the seabed responses, including pore fluid pressure and soil skeleton motion, are obtained. The present solutions are suitable for general transient wave loading and for the shear modulus of the soil skeleton being of the same order of magnitude as the effective bulk modulus of elasticity of the pore fluid. The present theory is first validated by checking the solutions with the experimental data for the pore pressure induced by periodic-wave loading. The present analytical solutions are then used to investigate the seabed responses under transient waves, including linear periodic wave, a solitary wave and a bore. The effects of the wave-induced effective stresses on the bed failure potential are further analysed. The results show that the shear failure potential and its duration are highly dependent on the soil properties, such as saturation degree, shear modulus and permeability. Sensitivity analyses are presented.

Key words: coastal engineering, solitary waves, hydraulics

† Email address for correspondence: philip.liu@nus.edu.sg

1. Introduction

When water waves propagate into coastal regions, dynamic pressures will be generated and applied at the water–seabed interface, leading to variations in pore pressure and effective stresses inside the seabed (Terzaghi 1943; Baumgarten & Kamrin 2019). Because of the dynamic wave–seabed interaction, the seabed may become unstable. Phenomena such as scour, liquefaction and shear failure could occur under different conditions (Yamamoto 1977; Sumer & Fredsøe 2002). The occurrence of seabed instability has great impact on wave propagation, sediment transport and the safety of offshore structures (Jeng *et al.* 2013; Ragione *et al.* 2019; Tong *et al.* 2020).

Since the 1940s, a number of theories have been developed to investigate wave-induced dynamic seabed responses (Sumer 2014). In general, these theories are based on two kinds of physical conditions: either a rigid or a deformable seabed (Bear 1972). In the rigid seabed models, the soil skeleton is non-deformable and the flow is governed by the Laplace equation of the pore-pressure field if the compressibility of the pore fluid is further ignored (i.e. Darcy's flow model) (Putnam 1949; Liu 1973; Liu, Davis & Downing 1996; Body & Ehrenmark 1998). Otherwise, if the pore fluid's compressibility is significant, the diffusion equation of the pressure governs the corresponding pore flow (Moshagen & Tørum 1975; Tørum 2007). Although the seabed is likely to be highly saturated, the apparent bulk modulus of elasticity of the pore fluid, K, decreases drastically if the pore water contains a very small amount of air. For instance, K decreases by four orders of magnitude if the degree of saturation, S_r, is reduced from 1 to 0.95 at atmospheric pressure (Yamamoto *et al.* 1978).

When the soil deformation has considerable influence on the flows inside and over the seabed (Wen & Liu 1995; Abdolali, Kadri & Kirby 2019), deformable medium models are required (Biot 1941; Madsen 1978). The mechanical properties of the soil skeleton are associated with several parameters, such as the grain size, degree of consolidation and loading pattern. To consider the deformation of the soil, the strain–stress relationship must be known. For a well-consolidated sandy bed, wave-induced soil deformation is relatively small, and therefore Hooke's law is widely used to describe the constitutive relationship (Baumgarten & Kamrin 2019; Hsu, Chen & Tsai 2019), which has been confirmed by field and laboratory measurements (Zen & Yamazaki 1991; Zhai *et al.* 2018; Qi *et al.* 2019). However, for a loose silty or clayey bed, elastoplastic models are more appropriate (Rahman, Lo & Dafalias 2014; Meyer, Langford & White 2016; Zhao *et al.* 2020).

Within the framework of the poroelastic theory and the linear wave assumption, analytical solutions for the displacements of the soil skeleton and pore pressure were first obtained by Yamamoto *et al.* (1978), in which the soil was assumed to be homogeneous and isotropic. Their solutions were applied to evaluate the shear failure potential inside the sandy seabed under the North Sea design conditions (Yamamoto 1978). Madsen (1978) derived similar analytical solutions for a hydraulically anisotropic seabed. Using the derived solutions, the shear failure inside a saturated seabed was examined under a storm condition. Note that the solutions of both Yamamoto *et al.* (1978) and Madsen (1978) were obtained by assuming that the seabed thickness was infinite. Mei & Foda (1981) obtained a one-dimensional exact solution for harmonic motion within a finite poroelastic seabed, in which the physical features of the shear waves were clarified. Based on these physical characteristics of the shear waves, a boundary layer theory was further developed, in which the drainage effect was only considered inside the boundary layer. Hsu & Jeng (1994) further derived analytical solutions for a seabed of finite thickness. Using the finite-thickness solutions, Jeng (1997) investigated wave-induced seabed instability,

including liquefaction and shear failure, in front of a perfectly reflecting seawall. In addition, new solutions were obtained by Jeng & Rahman (2000) and Ulker & Rahman (2009) to consider the effects of inertia forces. The comparisons showed that inertia forces may be more important in deeper water with larger thickness for a coarse sandy seabed (Jeng & Rahman 2000).

All the analytical studies mentioned above were derived for simple harmonic waves. However, transient waves such as solitary waves and bores can be observed in coastal and ocean regions (Chanson 2009; Chan & Liu 2012; Pujara, Liu & Yeh 2015) and they can cause seabed failure (Packwood & Peregrine 1980; Liu, Park & Lara 2007; Young, Xiao & Maddux 2010; Sumer *et al.* 2011; Jia *et al.* 2019; Tehranirad, Kirby & Shi 2020), suggesting that transient wave-induced pore pressure and effective stresses, and their effects on instability within a deformable seabed, require attention as well. According to our literature survey, only a few studies have been carried out on this topic (Young *et al.* 2009; Merxhani & Liang 2012; Rivera-Rosario, Diamessis & Jenkins 2017; Rivera-Rosario *et al.* 2020) and they are typically numerical approaches. Moreover, the assumptions employed in the governing equations used in the numerical studies are not clearly stated, which demands further attention.

In the present paper, we provide an analytical solution for pore pressure and soil effective stresses within an unsaturated poroelastic seabed under transient waves, focusing on the case where the thickness of the seabed is much smaller than the length scales of the water wave and soil shear wave. The motions of the fluid and soil skeleton are described by the consolidation theory, and the deformation of the soil skeleton obeys Hooke's law. With these assumptions, analytical solutions for the pore-pressure and soil responses are obtained once the time history of the dynamic pressure along the water–seabed interface is prescribed. Based on the present solutions, the dynamic and kinematic features inside the seabed under a linear wave train, a solitary wave and a bore are studied. As an application, the present theory is used for investigating the effects of wave-induced dynamic responses on shear failure inside the seabed under periodic waves and transient waves.

The remainder of this paper is organized as follows. After introducing the proper scales, the governing equations for the motions of pore fluid and soil skeleton, and the boundary conditions, are given in § 2. The analytical solutions for transient wave-induced pore-pressure and soil responses are derived in § 3. In § 4, the results of the present theory are checked with two laboratory experiments. Using the validated theory, the dynamic and kinematic responses within an unsaturated poroelastic seabed induced by a linear wave train, a solitary wave and a bore are investigated in § 5 The wave-induced shear failure potential and its effects are investigated in § 6. Finally, concluding remarks are provided in § 7.

2. Governing equations and boundary conditions

As shown in figure 1, transient water waves with characteristic amplitude a_0', characteristic wavelength l_0' and characteristic period T' propagate in water with constant depth h' lying over a seabed with thickness d'. Cartesian coordinates (x', z') are used on the vertical plane, with the origin on the still-water level.

The seabed is modelled as an unsaturated poroelastic medium, which is characterized by its shear modulus G, density ρ_s, permeability k_s and porosity n. Following Mei & Foda

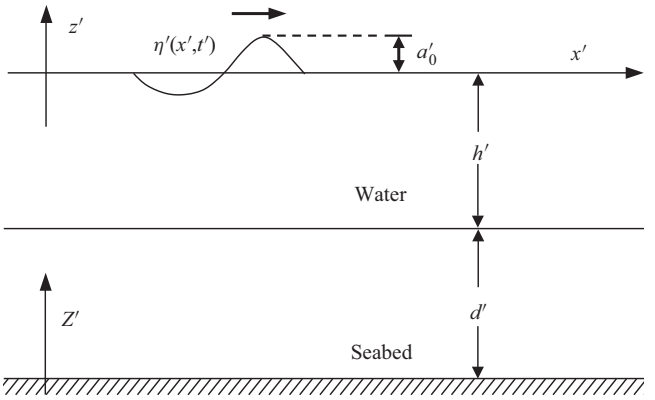

Figure 1. Sketch of a transient wave propagating over a seabed of finite thickness.

(1981), the dynamic responses inside the seabed are scaled as follows:

$$\left.\begin{aligned} x = \frac{x'}{l'_0}, \quad Z = \frac{1}{d'}(z' + d' + h'), \quad t = \frac{t'}{T'}, \\ (\kappa_1 u_f, w_f) = \frac{1}{\kappa_1 \gamma C'}(u'_f, w'_f), \quad (\kappa_1 u_s, w_s) = \frac{1}{\kappa_1 \gamma C'}(u'_s, w'_s), \\ p = \frac{1}{\rho_f g a'_0} p', \quad \boldsymbol{\tau}_{ij} = \frac{1}{\rho_f g a'_0}\boldsymbol{\tau}'_{ij}, \quad \boldsymbol{\varepsilon}_{ij} = \frac{1}{\gamma}\boldsymbol{\varepsilon}'_{ij}. \end{aligned}\right\} \tag{2.1}$$

Here, ρ_f is the density of the pore fluid, g represents the acceleration of gravity, $C' = l'_0/T'$ is the characteristic wave celerity, and (u_f, u_s) and (w_f, w_s) denote the dimensionless velocity components in the x- and z-directions, where the subscripts f and s denote the pore fluid and soil skeleton, respectively. In (2.1), $\gamma = \rho_f g a'_0/G$ is a dimensionless parameter characterizing the soil deformation, and

$$\kappa_1 = d'/l'_0 \tag{2.2}$$

represents the vertical to horizontal length ratio. Moreover, p is the wave-induced pore pressure, $\boldsymbol{\tau}_{ij}$ denotes the stress tensor and $\boldsymbol{\varepsilon}_{ij}$ represents the strain tensor. Tension is considered as positive for the analysis. The scales of the pore fluid and soil skeleton velocity are inferred from Hooke's law.

2.1. *Governing equations*

Based on the consolidation theory, the continuity equation for the soil skeleton can be expressed as (Yamamoto *et al.* 1978; see Appendix A herein)

$$\frac{\kappa_2^2}{\kappa_1^2}\frac{\partial^2 p}{\partial Z^2} - \frac{\partial w_s}{\partial Z} + \kappa_1^2\left(\frac{\kappa_2^2}{\kappa_1^2}\frac{\partial^2 p}{\partial x^2} - \frac{\partial u_s}{\partial x}\right) = n\frac{G}{K}\frac{\partial p}{\partial t}, \tag{2.3}$$

where κ_2 is a dimensionless parameter, being defined as

$$\kappa_2 = \frac{1}{l'_0}\sqrt{\frac{GT'k_s}{\rho_f v_f}}, \tag{2.4}$$

with v_f denoting the kinematic viscosity of the pore fluid. As suggested by Verruit (1969), the apparent bulk modulus of elasticity of the pore fluid, K, depends on the degree of saturation, S_r, as

$$\frac{1}{K} = \frac{1}{K_w} + \frac{1 - S_r}{p'_{abs}}, \tag{2.5}$$

where K_w is the bulk modulus of elasticity of pure water and p'_{abs} is the absolute pore-water pressure.

The leading-order equilibrium equations for the mixture of the pore fluid and soil skeleton are (e.g. Jeng 2003)

$$\kappa_1 \frac{\partial \tau_{xx}}{\partial x} + \frac{\partial \tau_{zx}}{\partial Z} - \kappa_1 \frac{\partial p}{\partial x} = 0 \tag{2.6}$$

in the horizontal direction, and

$$\kappa_1 \frac{\partial \tau_{xz}}{\partial x} + \frac{\partial \tau_{zz}}{\partial Z} - \frac{\partial p}{\partial Z} = 0 \tag{2.7}$$

in the vertical direction. Based on Hooke's law, the effective stresses are related to the strains as (e.g. Mei & Foda 1981)

$$\frac{\partial \tau_{xx}}{\partial t} = 2\left[\frac{\partial \varepsilon_{xx}}{\partial t} + \frac{\nu}{1 - 2\nu}\left(\frac{\partial \varepsilon_{xx}}{\partial t} + \frac{\partial \varepsilon_{zz}}{\partial t}\right)\right], \tag{2.8}$$

$$\frac{\partial \tau_{zx}}{\partial t} = \frac{\partial \tau_{xz}}{\partial t} = \frac{\partial \varepsilon_{xz}}{\partial t} = \frac{\partial \varepsilon_{zx}}{\partial t}, \tag{2.9}$$

$$\frac{\partial \tau_{zz}}{\partial t} = 2\left[\frac{\partial \varepsilon_{zz}}{\partial t} + \frac{\nu}{1 - 2\nu}\left(\frac{\partial \varepsilon_{xx}}{\partial t} + \frac{\partial \varepsilon_{zz}}{\partial t}\right)\right], \tag{2.10}$$

where ν is Poisson's ratio of the soil skeleton, and the dimensionless strain tensor can be determined by the linear geometric equation as

$$\left\{\frac{\partial \boldsymbol{\varepsilon}_{ij}}{\partial t}\right\} = \frac{\partial}{\partial t}\begin{pmatrix} \varepsilon_{xx} & \varepsilon_{zx} \\ \varepsilon_{xz} & \varepsilon_{zz} \end{pmatrix} = \begin{pmatrix} \kappa_1^2 \dfrac{\partial u_s}{\partial x} & \kappa_1 \dfrac{\partial u_s}{\partial Z} + \kappa_1 \dfrac{\partial w_s}{\partial x} \\ \kappa_1 \dfrac{\partial u_s}{\partial Z} + \kappa_1 \dfrac{\partial w_s}{\partial x} & \dfrac{\partial w_s}{\partial Z} \end{pmatrix}. \tag{2.11}$$

The above constitutive law for wave-induced soil skeleton responses inside a sandy seabed has been confirmed by both field observation data and laboratory measurements (Zen & Yamazaki 1991; Qi *et al.* 2019).

In addition, Darcy's law for the poroelastic seabed can be expressed as

$$\frac{\partial p}{\partial x} = -n\frac{\kappa_1^2}{\kappa_2^2}(u_f - u_s), \tag{2.12}$$

$$\frac{\partial p}{\partial Z} = -n\frac{\kappa_1^2}{\kappa_2^2}(w_f - w_s). \tag{2.13}$$

2.2. *Dimensionless boundary conditions*

At the bottom of the seabed, no-slip and no-flux boundary conditions are required (Mei & Foda 1981; Hsu & Jeng 1994). Thus

$$u_s = w_s = 0, \quad \frac{\partial p}{\partial Z} = 0, \quad \text{at } Z = 0. \tag{2.14a,b}$$

Along the water–seabed interface, the vertical effective stress vanishes, i.e.

$$\tau_{zz} = 0, \quad \text{at } Z = 1, \tag{2.15}$$

and the shear stress also vanishes,

$$\tau_{zx} = 0, \quad \text{at } Z = 1. \tag{2.16}$$

Finally, the dynamic water pressure must be continuous, namely,

$$p = p_b, \quad \text{at } Z = 1, \tag{2.17}$$

where p_b is the dimensionless dynamic water pressure at the water–seabed interface, which is the sole driving force of the seabed responses.

3. Analytical solutions inside a shallow unsaturated poroelastic seabed

In coastal regions, the thickness of the seabed varies over a wide range (Jeng 2003). In this paper, we are interested in the condition where d' is of the order of magnitude of $O(10\ \text{m})$. For transient long waves, such as solitary waves or bores, the wavelength, l'_0, can be of the order of magnitude of $O(10^2\ \text{m})$ or even longer, and therefore $O(\kappa_1^2) \ll 1$. For wind waves with typical period of $O(10\ \text{s})$, the wavelength is also of the order of magnitude of $O(10^2\ \text{m})$, and therefore the previous inequality is satisfied as well. For instance, under the North Sea design condition with $d' = 25$ m and $l'_0 = 324$ m (Yamamoto 1978), one has $\kappa_1^2 = 6 \times 10^{-3}$.

For a sandy seabed, the permeability k_s varies from 10^{-12} to $10^{-9}\ \text{m}^2$ (Body & Ehrenmark 1998), indicating that κ_2 can be of the same order of magnitude as the seabed thickness. As a rough estimate, consider typical sandy seabed conditions: $G = 10^7$ Pa, $k_s = 10^{-10}\ \text{m}^2$ and $d' = 10$ m. Then one has $\kappa_2^2/\kappa_1^2 = O(1)$ with $T' = 10$ s, and $\kappa_2^2/\kappa_1^2 = O(10)$ with $T' = 100$ s, suggesting that

$$O(\kappa_2^2) \sim O(\kappa_1^2) \ll 1, \tag{3.1}$$

where $l'_0 = gT'^2/(2\pi)$ and $\upsilon_f = 10^{-6}\ \text{m}^2\ \text{s}^{-1}$ are used for estimation. Finally, in this study, we shall focus on an unsaturated seabed, and under this condition G/K is usually much larger than κ_1^2. For example, consider the seabed with typical shear modulus of 10^7 Pa under a 10 m water column, then $G/K = O(1)$ when $S_r = 0.99$–0.95.

3.1. *Analytical solution for pore pressure*

Based on the approximations mentioned above, the governing equation for the pore pressure, (2.3), can be further simplified to

$$\frac{\partial w_s}{\partial Z} + n\frac{G}{K}\frac{\partial p}{\partial t} = \frac{\kappa_2^2}{\kappa_1^2}\frac{\partial^2 p}{\partial Z^2}, \quad 0 \le Z \le 1. \tag{3.2}$$

The combination of (2.9) and (2.11) shows that τ_{xz} is of the order of $O(\kappa_1)$. Therefore, applying the boundary condition (2.15), equation (2.7) can be simplified to the

one-dimensional principle of effective stress, namely $\tau_{zz} - p = -p_b$. In addition, applying the approximation (3.1) in the constitutive law (2.10) and the geometric equation (2.11), we obtain

$$\frac{\partial w_s}{\partial Z} = \frac{1-2\nu}{2-2\nu}\frac{\partial (p-p_b)}{\partial t}, \quad 0 \le Z \le 1. \tag{3.3}$$

Finally, substituting the equation above into (3.2) yields

$$\alpha^2\left(\frac{\partial p}{\partial t} - \beta\frac{\partial p_b}{\partial t}\right) = \frac{\partial^2 p}{\partial Z^2}, \quad 0 \le Z \le 1, \tag{3.4}$$

in which α and β are constants, defined by

$$\alpha = \kappa_1\frac{\sqrt{\tilde{\nu}+\tilde{G}}}{\kappa_2}, \quad \beta = \frac{\tilde{\nu}}{\tilde{\nu}+\tilde{G}}, \quad \text{with } \tilde{\nu} = \frac{1-2\nu}{2-2\nu}, \quad \tilde{G} = n\frac{G}{K}. \tag{3.5a,b}$$

Equation (3.4) is a non-homogeneous one-dimensional diffusion equation, and $1/\alpha$ measures the diffusion depth of the wave-induced pore pressure. If the soil skeleton is assumed to be rigid, i.e. $G \to \infty$, then $\beta \to 0$ and $1/\alpha \to \sqrt{k_s K T'/(n\rho_f v_f)}/d'$. Consequently, (3.4) reduces to the one-dimensional diffusion equation used in Liu *et al.* (2007).

Introducing the intermediate variable $\mathcal{P}$, given by

$$\mathcal{P} = p - \beta p_b, \tag{3.6}$$

in (3.4), the boundary-value problem for p can be expressed in terms of $\mathcal{P}$ as

$$\alpha^2\frac{\partial \mathcal{P}}{\partial t} = \frac{\partial^2 \mathcal{P}}{\partial Z^2}, \quad 0 \le Z \le 1, \tag{3.7}$$

with the following boundary conditions:

$$\frac{\partial \mathcal{P}}{\partial Z} = 0, \quad \text{at } Z = 0, \tag{3.8}$$

$$\mathcal{P} = (1-\beta)p_b, \quad \text{at } Z = 1. \tag{3.9}$$

Assuming that the pressure field begins from a quiescent state, the initial two-point boundary-value problem (3.7), (3.8) and (3.9) can be solved by the Laplace transformation method, and the analytical solution can be readily expressed as

$$\mathcal{P} = (1-\beta)p_b + 2(1-\beta)\int_0^t \frac{\partial p_b}{\partial \vartheta}\left[\sum_{\ell=1}^{\infty}\frac{\mathscr{G}_\ell(t-\vartheta)}{a_\ell}\cos(a_\ell Z)\right]\mathrm{d}\vartheta, \tag{3.10}$$

in which a_ℓ are constants given by $(2\ell-1)\pi/2$, and $\mathscr{G}_\ell(t-\vartheta)$ is defined as

$$\mathscr{G}_\ell(t-\vartheta) = (-1)^\ell \exp[-a_\ell^2(t-\vartheta)/\alpha^2]. \tag{3.11}$$

According to (3.6), the solution of p can be straightforwardly written as

$$p = p_b + 2(1-\beta)\int_0^t \frac{\partial p_b}{\partial \vartheta}\left[\sum_{\ell=1}^{\infty}\frac{\mathscr{G}_\ell(t-\vartheta)}{a_\ell}\cos(a_\ell Z)\right]\mathrm{d}\vartheta. \tag{3.12}$$

For later use, the leading-order solutions for the wave-induced pore-pressure gradients in the horizontal and vertical directions are obtained as

$$\frac{\partial p}{\partial x} = \frac{\partial p_b}{\partial x} + 2(1-\beta)\int_0^t \frac{\partial^2 p_b}{\partial x \partial \vartheta}\left[\sum_{\ell=1}^{\infty}\frac{\mathscr{G}_\ell(t-\vartheta)}{a_\ell}\cos(a_\ell Z)\right]\mathrm{d}\vartheta \tag{3.13}$$

and

$$\frac{\partial p}{\partial Z} = -2(1-\beta)\int_0^t \frac{\partial p_b}{\partial \vartheta}\left[\sum_{\ell=1}^{\infty}\mathscr{G}_\ell(t-\vartheta)\sin(a_\ell Z)\right]\mathrm{d}\vartheta, \tag{3.14}$$

respectively.

3.2. *Analytical solutions for soil skeleton responses*

Combining (3.2) with (3.3) to eliminate $\partial p/\partial t$ yields

$$\frac{\partial w_s}{\partial Z} = \frac{\tilde{\nu}}{\alpha^2}\frac{\partial^2 p}{\partial Z^2} - \beta\tilde{G}\frac{\partial p_b}{\partial t}, \quad 0 \le Z \le 1. \tag{3.15}$$

Thus, the vertical velocity component of the soil skeleton can be obtained by integration as

$$w_s = -(1-\beta)\frac{2\tilde{\nu}}{\alpha^2}\int_0^t \frac{\partial p_b}{\partial \vartheta}\left[\sum_{\ell=1}^{\infty}\mathscr{G}_\ell(t-\vartheta)\sin(a_\ell Z)\right]\mathrm{d}\vartheta - \beta\tilde{G}\frac{\partial p_b}{\partial t}Z. \tag{3.16}$$

Substituting the solutions of p and w_s into (2.13), the vertical velocity component of the pore fluid can be expressed as

$$w_f = \frac{(1-\beta)(1-n\beta)}{n\beta}\frac{2\tilde{\nu}}{\alpha^2}\int_0^t \frac{\partial p_b}{\partial \vartheta}\left[\sum_{\ell=1}^{\infty}\mathscr{G}_\ell(t-\vartheta)\sin(a_\ell Z)\right]\mathrm{d}\vartheta - \beta\tilde{G}\frac{\partial p_b}{\partial t}Z. \tag{3.17}$$

According to the one-dimensional principle of effective stress, $\tau_{zz} - p = -p_b$, the wave-induced vertical effective stress can be obtained as

$$\tau_{zz} = 2(1-\beta)\int_0^t \frac{\partial p_b}{\partial \vartheta}\left[\sum_{\ell=1}^{\infty}\frac{\mathscr{G}_\ell(t-\vartheta)}{a_\ell}\cos(a_\ell Z)\right]\mathrm{d}\vartheta. \tag{3.18}$$

Based on (2.8), (2.9) and (2.11), the horizontal effective stress and the shear stress can be simplified as

$$\frac{\partial \tau_{xx}}{\partial t} = \frac{2\nu}{1-2\nu}\frac{\partial w_s}{\partial Z}, \quad \frac{\partial \tau_{zx}}{\partial t} = \kappa_1\frac{\partial u_s}{\partial Z} + \kappa_1\frac{\partial w_s}{\partial x}. \tag{3.19a,b}$$

The combination of (3.19*a*,*b*) and (2.10) indicates that τ_{xx} is proportional to τ_{zz}, namely,

$$\tau_{xx} = \frac{\nu}{1-\nu}\tau_{zz} = 2(1-2\tilde{\nu})(1-\beta)\int_0^t \frac{\partial p_b}{\partial \vartheta}\left[\sum_{\ell=1}^{\infty}\frac{\mathscr{G}_\ell(t-\vartheta)}{a_\ell}\cos(a_\ell Z)\right]\mathrm{d}\vartheta. \tag{3.20}$$

Substituting (3.20) and (3.12) into (2.6) and employing the boundary condition (2.16), the shear stress can be calculated by integration as

$$\tau_{zx} = \tau_{xz} = 4\kappa_1\tilde{\nu}(1-\beta)\int_0^t \frac{\partial^2 p_b}{\partial x \partial \vartheta}\left[\sum_{\ell=1}^{\infty}\frac{\mathscr{G}_\ell(t-\vartheta)}{a_\ell}\frac{\mathscr{F}_\ell(Z)}{a_\ell}\right]\mathrm{d}\vartheta - \kappa_1(1-Z)\frac{\partial p_b}{\partial x}, \tag{3.21}$$

in which $\mathscr{F}_\ell(Z)$ is defined as

$$\mathscr{F}_\ell(Z) = (-1)^\ell + \sin(a_\ell Z). \tag{3.22}$$

The solutions show that τ_{xx} is of the same order of magnitude as τ_{zz}, which is of the order of unity, and τ_{zx} is of the order of κ_1, indicating that the shear stress is relatively weak for the case of a shallow seabed.

Combining (3.16) and (3.21) with (3.19*a*,*b*), the vertical gradient of horizontal velocity component of the soil skeleton is determined as

$$\begin{aligned}\frac{\partial u_s}{\partial Z} = &\left\{(1+\beta\tilde{G})Z - 1 + 4\tilde{\nu}(1-\beta)\sum_{\ell=1}^{\infty}\left[\frac{\mathscr{G}_\ell(0)}{a_\ell}\frac{\mathscr{F}_\ell(Z)}{a_\ell}\right]\right\}\frac{\partial^2 p_b}{\partial x\partial t}\\ &-(1-\beta)\frac{2\tilde{\nu}}{\alpha^2}\int_0^t \frac{\partial^2 p_b}{\partial x\partial\vartheta}\left\{\sum_{\ell=1}^{\infty}\mathscr{G}_\ell(t-\vartheta)[(-1)^\ell + \mathscr{F}_\ell(Z)]\right\}\mathrm{d}\vartheta.\end{aligned} \tag{3.23}$$

Thus, from the above equation, the horizontal velocity component of the soil skeleton can be calculated by integration as

$$\begin{aligned}u_s = &\left\{\frac{1}{2}(1+\beta\tilde{G})Z^2 - Z + 4\tilde{\nu}(1-\beta)\sum_{\ell=1}^{\infty}\left[\frac{\mathscr{G}_\ell(0)}{a_\ell}\frac{\mathscr{A}_\ell(Z)}{a_\ell}\right]\right\}\frac{\partial^2 p_b}{\partial x\partial t}\\ &-(1-\beta)\frac{2\tilde{\nu}}{\alpha^2}\int_0^t \frac{\partial^2 p_b}{\partial x\partial\vartheta}\left\{\sum_{\ell=1}^{\infty}\mathscr{G}_\ell(t-\vartheta)[(-1)^\ell Z + \mathscr{A}_\ell(Z)]\right\}\mathrm{d}\vartheta,\end{aligned} \tag{3.24}$$

where $\mathscr{A}_\ell(Z)$ is defined by

$$\mathscr{A}_\ell(Z) = \int_0^Z \mathscr{F}_\ell(\sigma)\,\mathrm{d}\sigma = (-1)^\ell Z + \frac{1-\cos(a_\ell Z)}{a_\ell}. \tag{3.25}$$

Finally, according to the horizontal momentum equation for the pore fluid, (2.12), the horizontal velocity component u_f is determined as

$$\begin{aligned}u_f = &\left\{\frac{1}{2}(1+\beta\tilde{G})Z^2 - Z + 4\tilde{\nu}(1-\beta)\sum_{\ell=1}^{\infty}\left[\frac{\mathscr{G}_\ell(0)}{a_\ell}\frac{\mathscr{A}_\ell(Z)}{a_\ell}\right]\right\}\frac{\partial^2 p_b}{\partial x\partial t}\\ &-(1-\beta)\frac{2\tilde{\nu}}{\alpha^2}\int_0^t \frac{\partial^2 p_b}{\partial x\partial\vartheta}\left\{\sum_{\ell=1}^{\infty}\mathscr{G}_\ell(t-\vartheta)[(-1)^\ell Z + \mathscr{A}_\ell(Z)]\right\}\mathrm{d}\vartheta\\ &-\frac{1}{n\beta}\frac{\tilde{\nu}}{\alpha^2}\left\{\frac{\partial p_b}{\partial x} + 2(1-\beta)\int_0^t \frac{\partial^2 p_b}{\partial x\partial\vartheta}\left[\sum_{\ell=1}^{\infty}\frac{\mathscr{G}_\ell(t-\vartheta)}{a_\ell}\cos(a_\ell Z)\right]\mathrm{d}\vartheta\right\}.\end{aligned} \tag{3.26}$$

4. Comparisons between analytical solutions and experimental data

On the basis of (3.12)–(3.14), the pore pressure and its gradients, induced by transient or periodic waves, can be calculated if the dynamic water pressure at the water–seabed interface is prescribed. In this section, the analytical solutions of pore pressure are first compared with laboratory experiments, including the one-dimensional water–soil column experiments reported by Liu & Jeng (2013) and Liu *et al.* (2015), and the periodic wave–seabed interaction experiments reported by Anderson *et al.* (2017). The experimental conditions are listed in table 1.

Physical parameters	Liu & Jeng (2013) Case I	Liu *et al.* (2015) Case II	Anderson *et al.* (2017) 2-D case
Water depth h' (m)	5.2	5.2	1.0
Wave period T' (s)	9.0	9.0	7.0
Wave amplitude a_0' (m)	0.62	1.75	0.375
Wave length l_0' (m)	61.7	61.7	26
Soil depth d' (m)	1.8	1.8	0.18
Soil porosity n	0.425	0.425	0.40
Poisson's ratio ν	0.3	0.3	0.35
Saturation degree S_r	0.975	0.996	0.982
Permeability coefficient k_s (m^2)	1.8×10^{-11}	1.8×10^{-11}	2.85×10^{-10}
Bulk modulus of elasticity of pore fluid K (Pa)	2.05×10^{6}	1.27×10^{7}	5.4×10^{5}
Shear modulus of the seabed G (Pa)	6.0×10^{6}	2.5×10^{8}	8.0×10^{6}
Dimensionless parameter κ_1^2	8.5×10^{-4}	8.5×10^{-4}	4.8×10^{-5}
Dimensionless parameter κ_2^2	2.6×10^{-4}	1.1×10^{-2}	2.4×10^{-2}

Table 1. Summary of physical conditions in the water–soil column experiments and wave–seabed interaction experiments.

4.1. *One-dimensional water–soil column experiment*

In the present section, we compare the analytical solution with the experimental data reported in Liu & Jeng (2013) (case I) and Liu *et al.* (2015) (case II), in which experiments were conducted in a vertical cylinder containing a 0.2 m column of water above a 1.8 m soil layer. Air pressure was applied on the water surface, comprising static and sinusoidal dynamic loads. The static load was equivalent to the static weight of a 5 m water column and the dynamic load corresponded to the dynamic water pressure induced by water waves, whose characteristics are listed in table 1. In the table, the wavelength is equivalent to that of a linear wave with period of 9 s in 5.2 m water depth. The soil used in the experiments was fine sand with a mean grain diameter, d_{50}, of 0.157 mm. The pore pressure along the vertical direction was measured by 10 pore-pressure transducers.

In both cases, the soil shear moduli are not directly measured. However, since the sand is loosely deposited in case I and is very similar to the loose sand used in Zhai *et al.* (2018), we adopt the same shear modulus value as 6×10^6 Pa. In case II, the experimental data are obtained after 3000 cycles of wave loading, suggesting that the sand bed is in a densely packed state. Therefore, the shear modulus is assumed to be 2.5×10^8 Pa, which is of the same order of magnitude as the shear modulus reported by Yamamoto *et al.* (1978) for dense sand. The dimensionless parameters shown in table 1 indicate that the assumptions invoked in the present study are well satisfied.

Figure 2 shows the vertical profiles of the maximum wave-induced pore pressure in the seabed. For comparison, the analytical results by Liu *et al.* (2007), which assumes $G \gg K$, are displayed as well. The present solutions agree well with the experimental data in both cases. The difference between the measurements and solutions may be caused by the higher-order solutions. On the other hand, the Liu *et al.* (2007) solutions agree well only with the experimental data in case II, which is densely packed sand. Therefore, soil deformation plays an important role and should be considered when the shear modulus of soil, G, is close to the apparent bulk modulus of elasticity of the pore fluid, K.

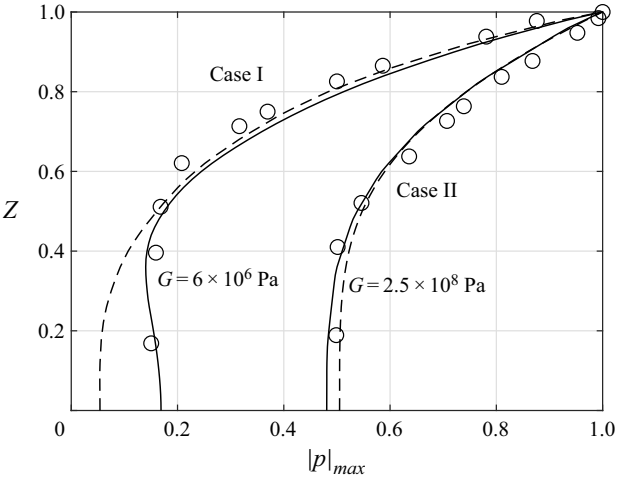

Figure 2. Vertical profiles of the maximum wave-induced pore pressure in case I of Liu & Jeng (2013) and case II of Liu *et al.* (2015). Circles, experimental results; solid lines, the present solution at leading order; and dashed lines, the previous solution without considering the deformation of the soil skeleton (Liu *et al.* 2007). Physical parameters are given in table 1.

4.2. *Periodic wave–seabed interaction experiments*

Anderson *et al.* (2017) conducted a set of experiments in the large wave flume at Oregon State University (the O.H. Hinsdale Wave Research Laboratory). The wave flume is 104 m long, 3.7 m wide and 4.6 m deep (Mieras *et al.* 2017). A barred beach profile was constructed based on the field surveys during the Duck94 experiments, as shown in figure 3(*a*). The main portion of the barred beach profile comprised concrete slabs. However, at the crest of the bar profile, a pit with 3.66 m $\times$ 3.66 m horizontal cross-section was filled with 0.18 m thick sediment. At the centre of the pit, a deeper chamber with a 1.20 m $\times$ 1.20 m cross-section and 0.43 m depth was installed to accommodate instruments. The still-water depths at the wavemaker and over the sandbar were 2.448 m and 1 m, respectively. To collect pore pressures, seven pore-pressure transducers were mounted in a T-shaped moulding with 2 cm spacing (centre-to-centre). The horizontal row has five transducers (P1–P5) and the vertical column adds two transducers (P6 and P7), as shown in figure 3(*b–d*). The pressure gradients at P3 are estimated by employing the finite-difference formulae using the measured pressures in the proximity.

The experimental wave conditions and the seabed soil properties are summarized in table 1. The wavelength is determined by the wave steepness given in Anderson *et al.* (2017), and the permeability of the soil is calculated by using the Kozeny–Carman equation (Bear 1972),

$$k_s = \frac{d_{50}^2 n^3}{180(1-n)^2}. \tag{3.1}$$

In the experiments, d_{50} is measured to be 0.17 mm. The porosity of the seabed and the density of the soil particles are not provided in Anderson *et al.* (2017). Here, we use the same values as those recommended in Kim *et al.* (2019).

Although the dynamic water pressure at the water–seabed interface was not directly measured in Anderson *et al.* (2017), it can be inferred from the time histories of the phase-averaged free-surface elevation, η', measured at the edge of the sand pit.

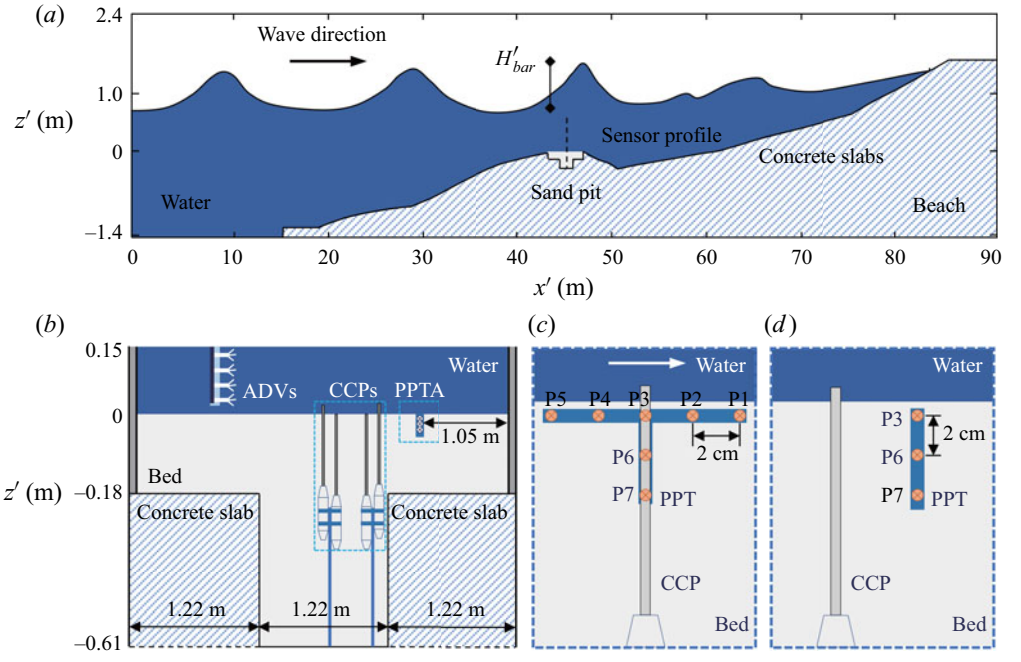

Figure 3. Experimental set-up and instrument layout in Anderson *et al.* (2017): (*a*) beach profile and sand pit; (*b*) illustration of the instrument configuration (including the acoustic Doppler velocimeters (ADVs), the conductivity concentration profilers (CCPs) and the pore-pressure transducer array (PPTA)), looking towards the beach; (*c*) the spanwise view of the PPTA and CCP in the sandy bed; and (*d*) the onshore view of sensor proximities.

For shallow-water waves (i.e. $h'/l'_0 = 0.046$), the pressure along the water–seabed interface, p'_b, can be approximated as $\rho_f g \eta'$. Moreover, the horizontal pressure gradient on the water–seabed interface, $\partial p_b/\partial x$, can be related to its time derivative, $\partial p_b/\partial t$. The degree of saturation is assumed to be 0.982, and the shear modulus, G, is set to be 8×10^6 Pa, which is the same as the measured value in Zhai *et al.* (2018) for a soil sample with a mean grain diameter of 0.15 mm, similar to the experiments of Anderson *et al.* (2017). These values are also listed in table 1.

In figure 4, the present theoretical results for the time histories of free-surface elevation at the offshore edge of the sandbar, the wave-induced horizontal pore-pressure gradient and the vertical pressure gradient at P3 are plotted against the laboratory measurements. The experimental data are represented by the phase-averaged value over 10 wave cycles and the error bar with one standard deviation. Since the dynamic pressure on the water–soil interface is linearly proportional to the free-surface elevation, figure 4(*a*) can be viewed as the time history of the dynamic pressure on the water–soil interface. Therefore, the horizontal pressure gradient is almost zero under the wave crest as shown in figure 4(*b*); a slight phase lag is observed because measurement is 0.9 cm below the water–soil interface. Overall, the agreement between the theoretical results and measurements is very good. Some differences in the pressure gradients occur during the receding phase of the water level. As reported by Anderson *et al.* (2017), the closest wave gauge to the sandy bed instruments was located at the offshore edge of the sandbar, 1.82 m from the pore-pressure transducers, and therefore the disagreement may be caused by the difference between

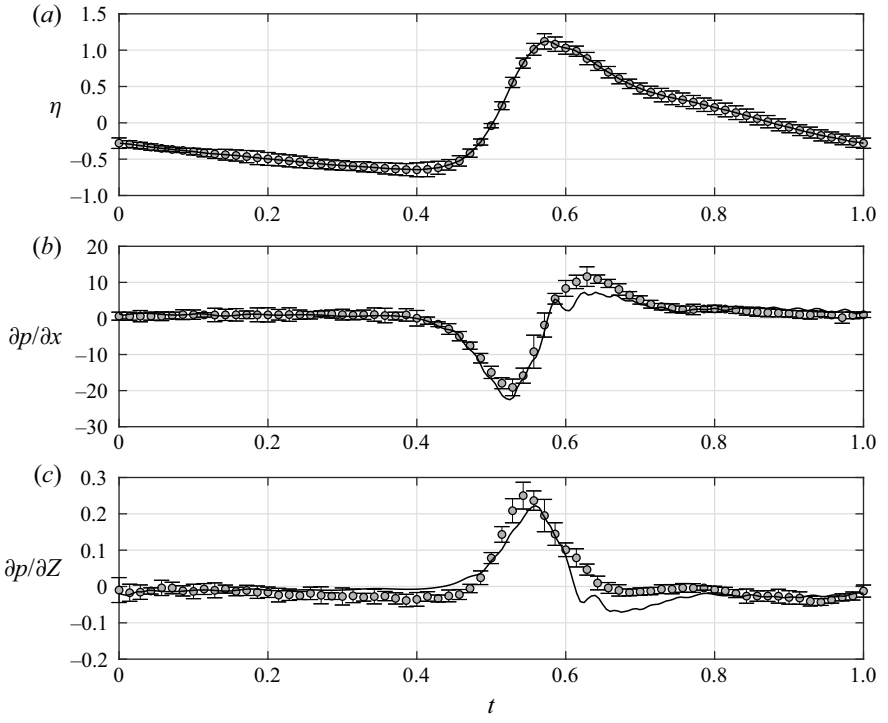

Figure 4. Time histories of (*a*) free-surface elevation at the offshore edge of the sandbar, (*b*) wave-induced pore-pressure gradient in the horizontal direction at 0.9 cm below the water–seabed interface, and (*c*) wave-induced pore-pressure gradient in the vertical direction. Grey dots, phase-averaged experimental results; error bars, standard deviation; black line, the present solutions with the physical parameters listed in table 1.

the waveform of the free surface at the offshore edge of the sandbar and that over the instruments.

Since the degree of saturation and the shear modulus are not directly measured in the experiments, the sensitivity of these two parameters to the wave-induced pressure gradients is further examined. The order of magnitude of G is set in the range of 10^4 to 10^7 Pa and the degree of saturation is set to 0.98, so that $K = 4.9 \times 10^5$ Pa. Figure 5 shows the calculated horizontal and vertical pressure gradients at 0.9 cm below the water–seabed interface. The differences between the solutions using shear modulus values of 10^6 and 10^7 Pa, respectively, are very small, because the soil is relatively dense, i.e. $G > K$, and the soil deformation is minor in both cases. However, when the shear modulus is further reduced, $1 - \beta$, which controls the amplitude of the vertical pressure gradient, decreases quickly, and α^2, which measures the diffusion time scale of the pressure, increases significantly. As a result, the vertical pressure gradient decreases rapidly and the phase lag also increases. Finally, according to Liu *et al.* (2007), the degree of saturation in soil has a significant influence on the pore-pressure response. To demonstrate this feature, wave-induced pressure gradients at 0.9 cm below the interface are plotted for $S_r = 0.97$, 0.98 and 0.99 in figure 6. Since P3 is close to the water–seabed interface, its horizontal pressure gradient is close to $\partial p_b/\partial x$ and not very sensitive to the change of saturation degree. However, the vertical pressure gradient increases rapidly with decreasing S_r, but the phases almost remain the same, since $1 - \beta$ increases and α^2 changes are small.

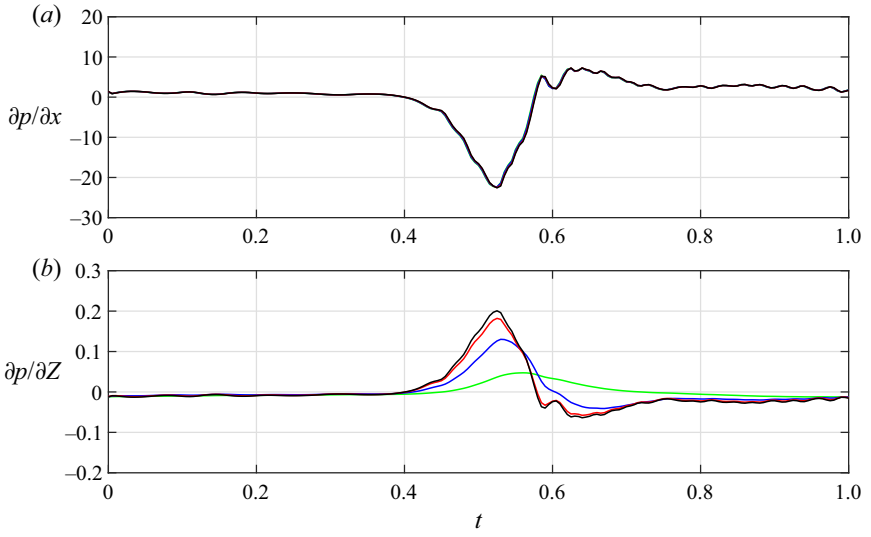

Figure 5. Time histories of wave-induced pressure gradients at 0.9 cm below the water–seabed interface: (*a*) the horizontal gradient and (*b*) the vertical gradient. Green line, $G = 1 \times 10^4$ Pa; blue line, $G = 1 \times 10^5$ Pa; red line, $G = 1 \times 10^6$ Pa; and black line, $G = 1 \times 10^7$ Pa. The other parameters used for calculation are listed in table 1.

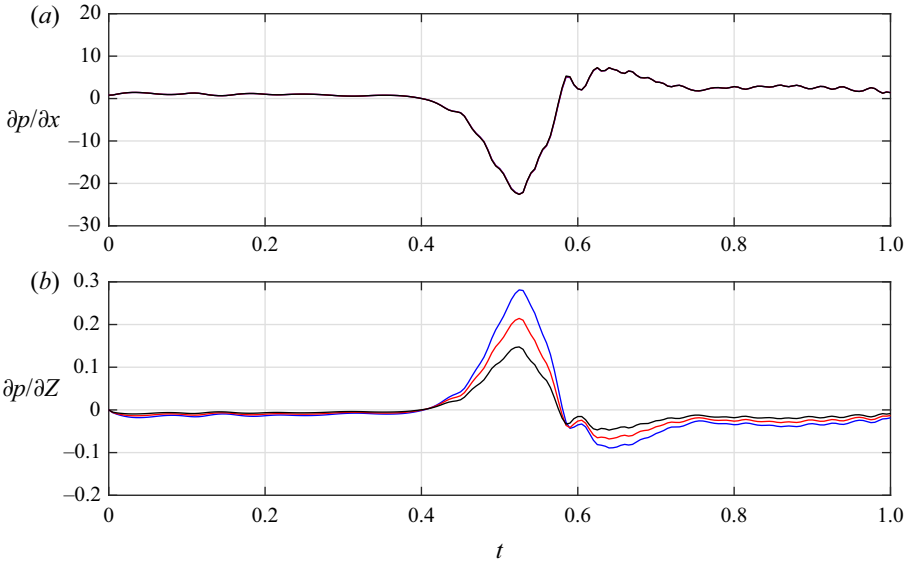

Figure 6. Time histories of wave-induced pressure gradients at 0.9 cm below the water–seabed interface: (*a*) the horizontal gradient and (*b*) the vertical gradient. Black line, $S_r = 0.99$; red line, $S_r = 0.98$; and blue line, $S_r = 0.97$. The other parameters used for calculation are listed in table 1.

5. Transient wave-induced soil responses within the seabed

In this section, the present analytical solutions are used to study the dynamic responses inside an unsaturated seabed under different transient wave loadings, including linear periodic waves, solitary waves and bores. The results are obtained by assigning

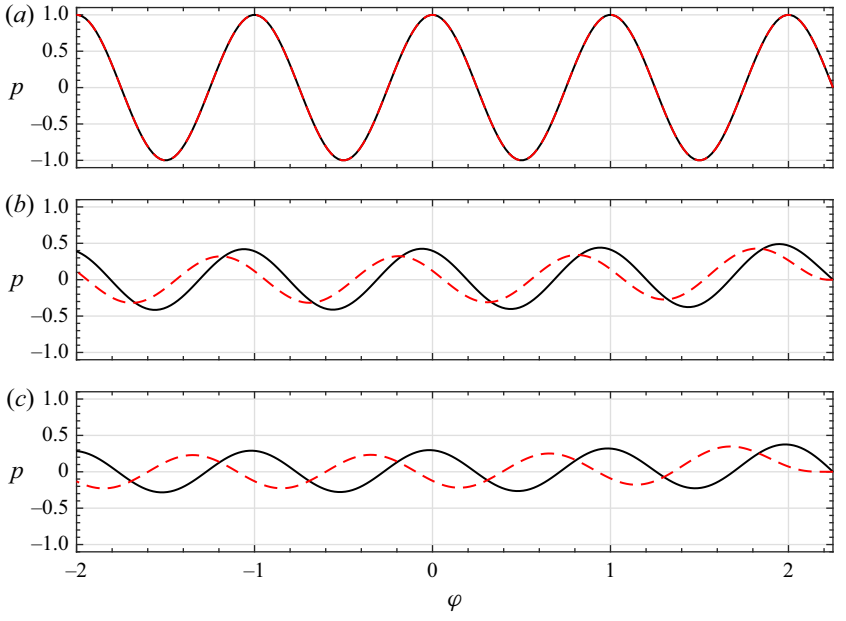

Figure 7. Time histories of the linear periodic-wave-induced dimensionless pore pressure within an unsaturated poroelastic seabed at three different elevations: (*a*) $Z = 1$ on the seabed–water interface, (*b*) $Z = 0.5$ at mid-depth of the seabed, and (*c*) $Z = 0$ on the seabed bottom. Black solid lines, the present solution (3.12); and red dashed lines, the solution of Liu *et al.* (2007) for rigid soil skeleton. The following parameters are used for calculation: $n = 0.45$, $\nu = 0.33$, $G = K = 2 \times 10^7$ Pa, $k_s = 1 \times 10^{-10}$ m^2, $\rho_f = 1 \times 10^3$ kg m^{-3}, $\upsilon_f = 1 \times 10^{-6}$ m^2 s^{-1}, $d' = 10$ m, $h' = 30$ m, $T' = 15$ s and $a'_0/h' = 0.1$.

$d' = 10$ m, $k_s = 1 \times 10^{-10}$ m^2, $G = K = 2 \times 10^7$ Pa, $\nu = 0.33$ and $n = 0.45$. Such a shallow medium sandy seabed is observed in the coastal region of Fujian, China (Wang & Yang 2019).

5.1. *Linear periodic-wave-induced pore-pressure and soil responses*

The analytical solutions for the pore pressure and its gradients induced by sinusoidal dynamic loads have been validated with experimental data in the previous section. Here we provide a general and broader discussion for linear periodic-wave-induced soil responses under typical wind wave conditions: $h' = 30$ m, $T' = 15$ s and $a'_0/h' = 0.1$. Based on the dispersion relationship of linear waves, $l'_0 = 234$ m, accordingly $\kappa_1^2 = 1.8 \times 10^{-3}$ and $\kappa_2^2 = 5.5 \times 10^{-4}$. In figure 7, the time histories of pressure p are plotted at three different elevations, $Z = 1.0$, 0.5 and 0, respectively.

For convenience and consistency, a moving coordinate is used in the analysis hereinafter. In figure 7, φ is a moving coordinate defined by $\varphi = x - t$. To understand the effects of soil deformation on the pore-pressure response, the rigid skeleton solutions of Liu *et al.* (2007) are shown in the figure as well. Since the pressure field begins from the quiescent state, it takes some time to reach the quasi-steady state. As shown in figure 7, the wave-induced pore pressure damps with increasing soil depth, and a phase lag in the arrival of the maximum pore pressure between $Z = 1$ and $Z = 0.5$ is apparent. Since the diffusion depth of the pore pressure measured by $1/\alpha$ is 0.65, the vertical pressure gradient (or the drainage velocity) is small beneath the diffusion region, and the soil behaves like an elastic

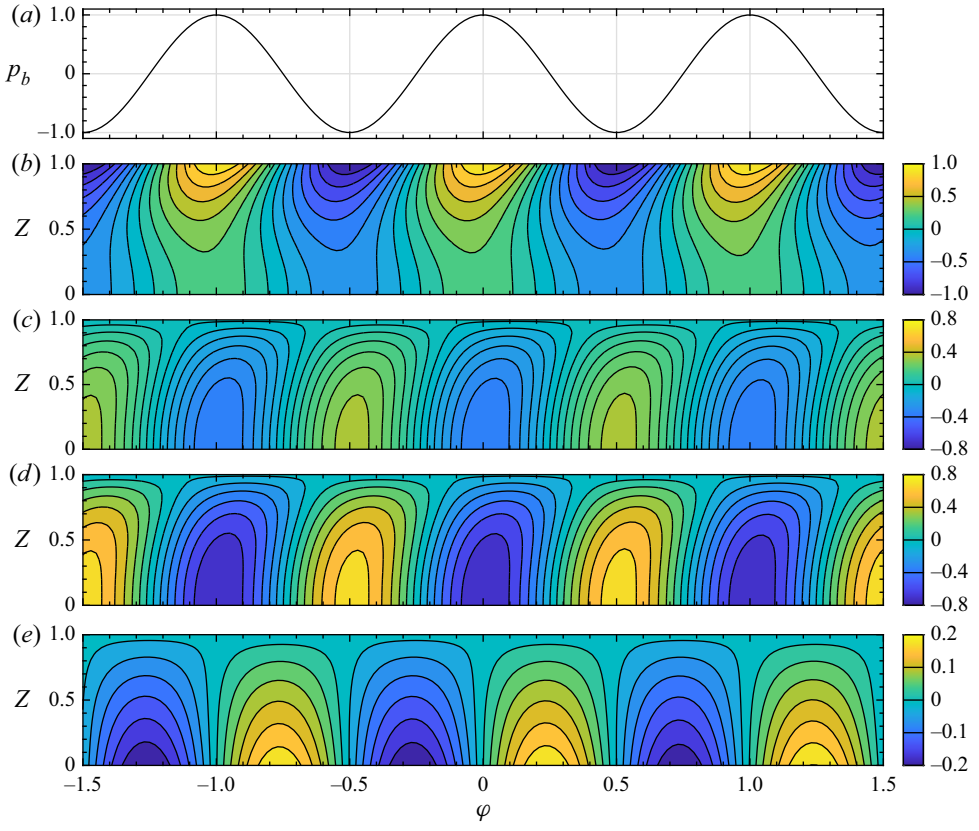

Figure 8. Contours of pore pressure and effective stresses inside a seabed: (*a*) the time history of the linear wave-induced dynamic water pressure at the water–seabed interface; (*b*) contours of the pore pressure p; (*c*) contours of the horizontal effective stress τ_{xx}; (*d*) contours of the vertical effective stress τ_{zz}; and (*e*) contours of the shear stress τ_{xz}. The physical parameters used in the calculation are given in the caption of figure 7.

solid (Mei & Foda 1981). Therefore, p approaches βp_b ($\beta = 0.36$) at the seabed bottom according to (3.4), and the phase lag in the arrival of the maximum pore pressure decreases to zero at $Z = 0$. However, without consideration of soil deformation, β decreases to zero, and therefore the amplitudes of the pore pressure in the seabed are smaller. In addition, the phase lags are longer and simply increase with increasing soil depth, since it always takes a longer time for the pressure to diffuse into a deeper location inside a rigid porous seabed.

Figure 8 shows the contours of the linear periodic-wave-induced pore pressure and effective stresses inside the seabed. The effective stresses vanish at the water–seabed interface as required by the boundary conditions, and the amplitudes of the effective stresses increase with increasing soil depth. The effective horizontal normal stress, τ_{xx}, and shear stress, τ_{xz}, are smaller than the effective vertical normal stress, τ_{zz}. Under the wave crest, the pressure reaches a maximum value at the water–seabed interface and damps with increasing soil depth, resulting in a negative vertical pressure gradient. Owing to this negative pressure gradient, the soil skeleton is compressed, and therefore a negative effective vertical normal stress (compression) is generated within the seabed. As the crest passes, the wave-induced pore pressure at the interface decreases on the interface and

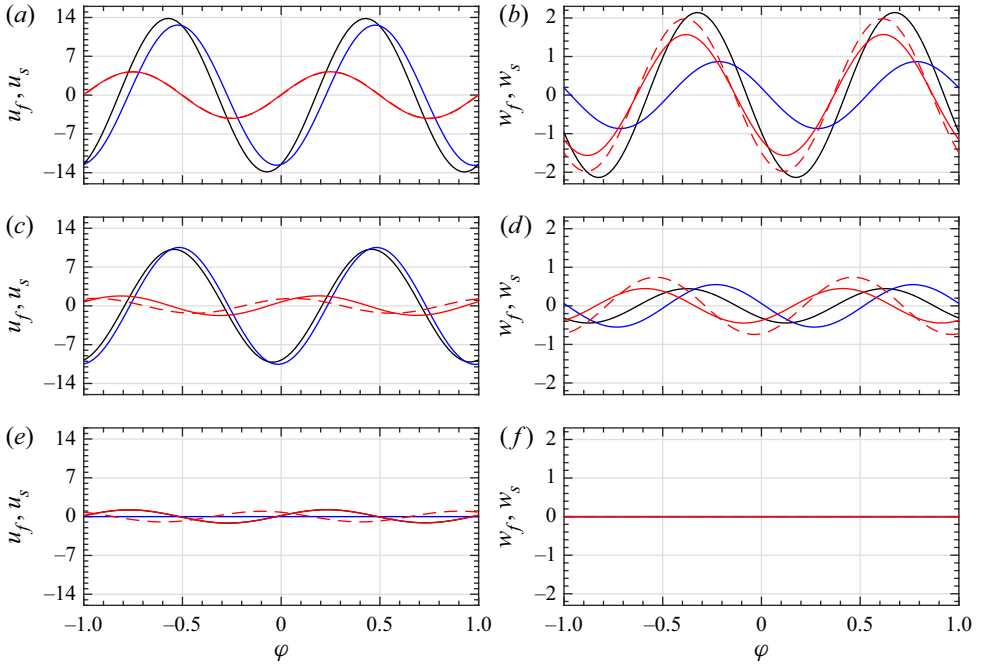

Figure 9. Time histories of linear wave-induced dimensionless velocity components at three different elevations, (*a*,*b*) $Z = 1$, (*c*,*d*) $Z = 0.5$ and (*e*,*f*) $Z = 0$, within an unsaturated poroelastic seabed. Black solid lines, the pore fluid velocity components; blue solid lines, the soil skeleton velocity components;red solid lines, the velocity difference of the pore fluid and soil skeleton calculated by the present solutions; and red dashed lines, the velocity difference of the pore fluid and soil skeleton calculated by Liu *et al.* (2007) for a rigid soil skeleton. The physical parameters used in the calculation are given in the caption of figure 7.

increases within the seabed. Consequently, the vertical pressure gradient increases and changes sign before the arrival of the wave trough. Therefore, a positive effective vertical normal stress (tension) is generated inside the seabed under the trough. The tendency of the effective horizontal effective stress is the same as that of the effective vertical normal stress, since $\tau_{xx} \propto \tau_{zz}$ in a shallow seabed according to (3.20). In addition, the shear stress, τ_{xz}, is positive in the ascending phase and negative in the receding phase. Lastly, the linear wave-induced pore pressure and effective stresses are symmetric.

Figure 9 displays the time histories of dimensionless velocity components of the pore fluid, (3.17) and (3.26), and the soil skeleton, (3.16) and (3.24), at three different elevations, $Z = 1.0$, 0.5 and 0, in which the left column shows the horizontal velocity components and the right column shows the vertical velocity components. For clarity, detailed vertical profiles of the velocity components at four different phases during the third wave period are also plotted in figure 10.

Since the shear modulus of the soil, G, equals the effective bulk modulus of elasticity of the pore fluid, K, under the present soil properties, the amplitudes of the velocity components of the soil skeleton at $Z = 1.0$ and $Z = 0.5$ are no longer negligible, compared with those of the pore fluid. At the bottom of the seabed, $Z = 0$, the velocity components of the soil skeleton vanish, determined by the boundary conditions. The horizontal velocity component of the pore fluid is negative under the crest and positive under the trough. The horizontal velocity component of the soil skeleton shows similar features; however, it reverses its direction before the horizontal velocity component of the the pore fluid changes

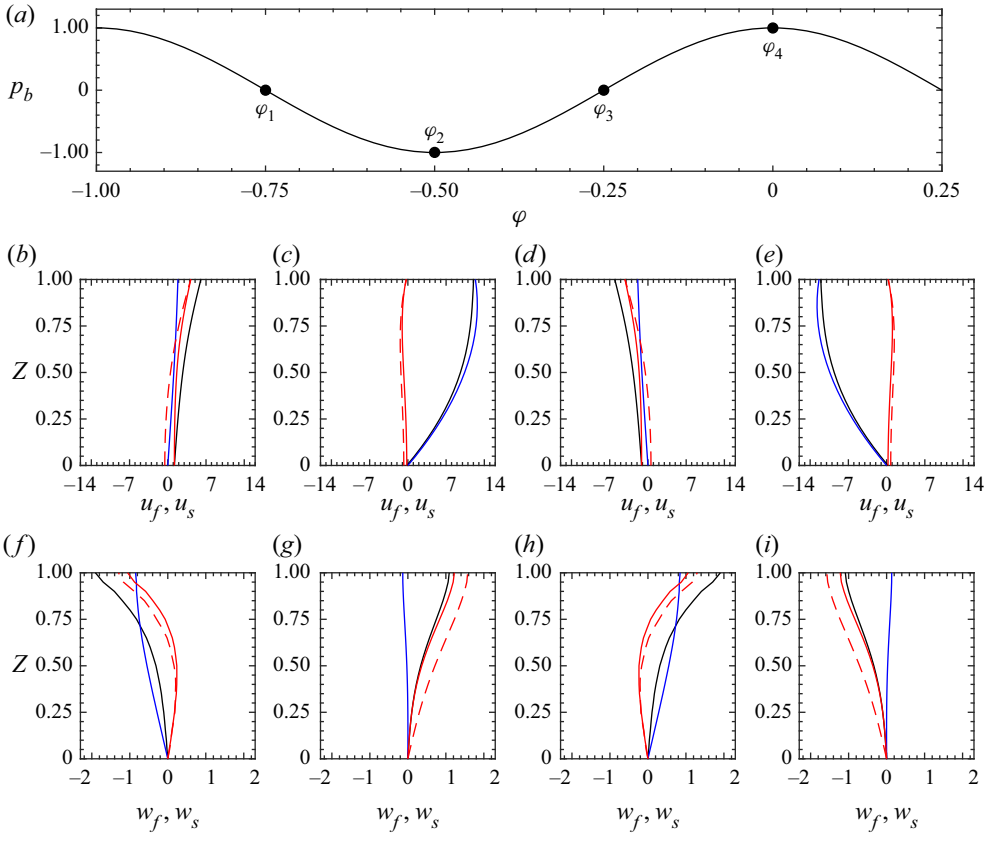

Figure 10. Vertical profiles of the dimensionless velocity components of the pore fluid, the soil skeleton and the seepage flow at four different phases: (*a*) the time history of the dynamic water pressure at the water–seabed interface; (*b–e*) the vertical profiles of the horizontal velocity components at $\varphi_1 = -0.75$, $\varphi_2 = -0.50$, $\varphi_3 = -0.25$ and $\varphi_4 = 0$, respectively; and (*f–i*) the vertical profiles of the vertical velocity components at $\varphi_1 = -0.75$, $\varphi_2 = -0.50$, $\varphi_3 = -0.25$ and $\varphi_4 = 0$, respectively. Black solid lines, the pore fluid velocity components; blue solid lines, the soil skeleton velocity components; red solid lines, the differences of the pore fluid and soil skeleton velocities calculated by the present solutions; and red dashed lines, the difference of the pore fluid and soil skeleton velocities calculated by Liu *et al.* (2007). The physical parameters used in the calculation are given in the caption of figure 7.

its sign. In the vertical direction, the vertical velocity components for the pore fluid and soil skeleton are positive in the receding phase and negative in the ascending phase, and the vertical velocity component of the soil skeleton also changes its direction before that of the pore fluid.

In addition, the vertical profiles of the velocity components are symmetric with respect to the wave crest and the wave trough, as shown in figure 10. The relative velocities between the pore fluid velocity and the soil skeleton velocity are compared in this figure as well. Recall that the soil skeleton in Liu *et al.* (2007) is rigid, and therefore the relative velocities and the seepage flow velocities calculated in Liu *et al.* (2007) are identical. The results show that the relative horizontal velocities are relatively small except near the bottom of the seabed, compared with the horizontal velocities of the pore fluid and soil skeleton. At the seabed bottom, the horizontal velocity component of the soil skeleton will be zero as required by the boundary condition, and therefore the relative horizontal

velocity component is the same as the horizontal velocity component of the pore fluid. As can be seen from figure 10, both the amplitudes and phases of the relative velocity components in the present solution and the solution of Liu *et al.* (2007) are different inside the seabed. This can be attributed to the fact that the pressure calculated from these two theories are different within the seabed (see figure 7), and $\nabla p \propto \boldsymbol{u}_f - \boldsymbol{u}_s$, (2.12) and (2.13), is true from both theories.

In the poroelastic seabed model, the discharge volume of pore fluid, $n\partial w_f/\partial Z$, is equal to the total compression volume of the soil skeleton, $\partial w_s/\partial Z$, and the pore fluid, $\tilde{G}\partial p/\partial t$, based on (3.2) and (2.13). Under the present wave conditions and soil properties, the wave-induced vertical normal effective stress reaches up to 0.72 at the seabed bottom (see figure 8), and therefore, according to (2.10) and (2.11), the compression volume of the soil skeleton is considerable, compared with that of the pore fluid. However, in the rigid seabed model, the compression volume of the soil skeleton is assumed to be zero (Liu *et al.* 2007). Consequently, the various fluid velocities calculated from both theories are significantly different.

5.2. *Solitary-wave-induced pore-pressure and soil responses*

It is well known that the effective wavelength and wave period of a solitary wave can be expressed as (e.g. Dean & Dalrymple 1991)

$$l_0' = h'\sqrt{\frac{4h'}{3a_0'}} \quad \text{and} \quad T' = \frac{l_0'}{\sqrt{gh'}}, \tag{5.1a,b}$$

respectively, which have been used as the horizontal length scale and the time scale for the present problem. Recall that a_0' is the solitary-wave height and h' is the water depth. Correspondingly, the dimensionless dynamic water pressure at the water–seabed interface approximated by normalized free-surface elevation can be written as (Packwood & Peregrine 1980; Knowles & Yeh 2018)

$$p_b = \operatorname{sech}^2(x - Ct), \tag{5.2}$$

where C is the dimensionless wave celerity, defined as $C = \sqrt{1 + a_0'/h'}$, and a_0'/h' measures the wave nonlinearity. Substituting the above expressions into (3.12), (3.16)–(3.18), (3.20), (3.21), (3.24) and (3.26), respectively, the dynamic responses inside the seabed are obtained. To illustrate various physical features, the solitary-wave conditions are set to be $h' = 30$ m and $a_0'/h' = 0.2$ as an example.

In figure 11, the time histories of the wave-induced pore pressure are plotted at three different elevations in the seabed, $Z = 1.0$, 0.5 and 0, respectively. For a solitary wave, the moving coordinate, $\varphi = x - Ct$, is used. The solitary-wave loading at the water–seabed interface ($Z = 1$) is symmetric with respect to the wave crest ($\varphi = 0$). However, the profiles become asymmetric at the mid-depth ($Z = 0.5$) and the bottom of the seabed ($Z = 0$), since the soil responses have a memory of the history of the spatial variation of the wave loading. There are also phase lags in the arrival of the maximum pore pressure. In addition, the width of the asymmetric pressure distribution becomes wider towards the bottom of the seabed. The width is defined as the time interval within which the pore pressure is larger than 1 % of the maximum pressure amplitude. Without considering the deformation of the soil skeleton, the phase lags are longer inside the seabed as well.

Figure 12 shows the contours of the solitary-wave-induced pore pressure and effective stresses within the seabed. As shown in the figure, the amplitudes of the effective stresses

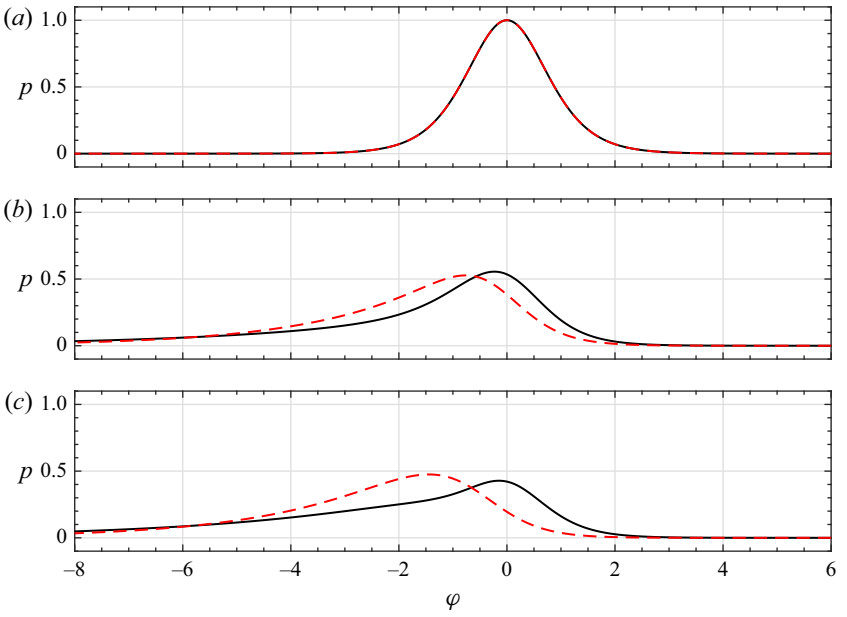

Figure 11. Time histories of the solitary-wave-induced dimensionless pore pressure within an unsaturated poroelastic seabed at three different elevations: (*a*) $Z = 1$ on the seabed–water interface; (*b*) $Z = 0.5$ at mid-depth of the seabed; and (*c*) $Z = 0$ on the seabed bottom. Black solid lines, the present solution (3.12); and red dashed lines, the solution of Liu *et al.* (2007) for a rigid soil skeleton. The following parameters are used for calculation: $\alpha = 2.79$, $\beta = 0.36$, $\kappa_1 = 3.33\kappa_2$ and $\tilde{\nu} = 0.25$. These correspond to the physical conditions: $n = 0.45$, $\nu = 0.33$, $G = K = 2 \times 10^7$ Pa, $k_s = 1 \times 10^{-10}$ m^2, $\rho_f = 1 \times 10^3$ kg m^{-3}, $\upsilon_f = 1 \times 10^{-6}$ m^2 s^{-1}, $d' = 10$ m, $h' = 30$ m and $a'_0/h' = 0.2$.

also increase with increasing soil depth. In the acceleration phase, the pressure inside the seabed damps with increasing soil depth, and therefore the soil is also compressed by the wave-induced pressure. After the wave crest, the dynamic water pressure at the interface decreases; however, due to the phase lag, the pressure within the seabed continues to increase. As a result, the pressure gradient changes sign from negative to positive, and a positive effective vertical normal stress is generated inside the seabed. Correspondingly, the effective shear stress changes sign in the opposite manner. Since the wave-induced pressure is relatively small at the seabed bottom, compared with the dynamic water pressure at the interface, the positive vertical pressure gradient in the deceleration phase is weak, and it takes a relatively long time to dissipate the wave-induced pressure and effective normal stresses.

Figure 13 further displays the time histories of dimensionless velocity components of the pore fluid and the soil skeleton at three different elevations, $Z = 1.0$, 0.5 and 0. The vertical profiles of the velocity components at five different phases are also plotted in figure 14. In the seabed, the horizontal velocity component of the pore fluid reverses its direction, first from positive to negative and then reverses it again from negative to positive after the horizontal pressure gradient changes its sign. The horizontal soil skeleton velocity behaves similarly, while its value is smaller in the acceleration phase and larger in the deceleration phase. However, the vertical velocity components show different features. Both the vertical velocity components of the pore fluid and soil skeleton simply reverse their directions from positive to negative before the vertical pressure gradient changes its sign with increasing φ. The relative velocities between the pore fluid velocity and the soil skeleton velocity are

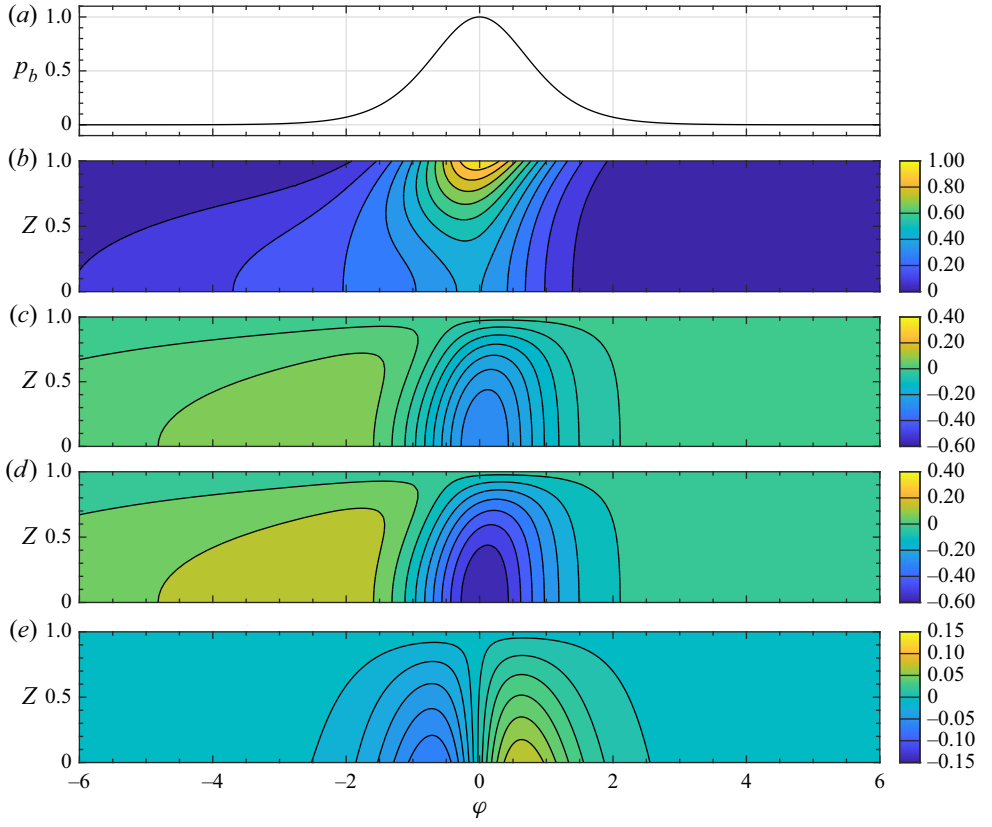

Figure 12. Contours of pore pressure and effective stresses inside a seabed: (*a*) the time history of the solitary-wave-induced dynamic water pressure at the water–seabed interface; (*b*) contours of the pore pressure p; (*c*) contours of the horizontal effective stress τ_{xx}; (*d*) contours of the vertical effective stress τ_{zz}; and (*e*) contours of the shear stress τ_{xz}. The physical parameters used in the calculation are given in the caption of figure 11.

compared in these figures as well. Owing to the wave-induced soil deformation within the seabed, the difference between the present solution and the solution of (Liu *et al.* 2007) is also obvious under a solitary wave.

5.3. *Bore-induced pore-pressure and soil responses*

According to Packwood & Peregrine (1980), the horizontal length scale and the time scale for a bore can be represented by (5.1*a*,*b*) as well. Thus, the bore-induced dimensionless dynamic water pressure at the water–seabed interface can be expressed as (Liu *et al.* 2007)

$$p_b = \tfrac{1}{2}[1 - \tanh(x - Ct)], \tag{5.3}$$

where C is the dimensionless bore velocity. Substituting (5.3) into the leading-order solutions for the pore pressure (3.12), the effective stresses (3.18), (3.20) and (3.21) and the velocity components of the pore fluid and soil skeleton (3.16), (3.17), (3.24) and (3.26), respectively, various features of seabed response under a bore can be obtained.

To quantify the results, the same set of physical parameters as employed in the previous subsection is used herein. In figure 15, time histories of the dimensionless pore pressure

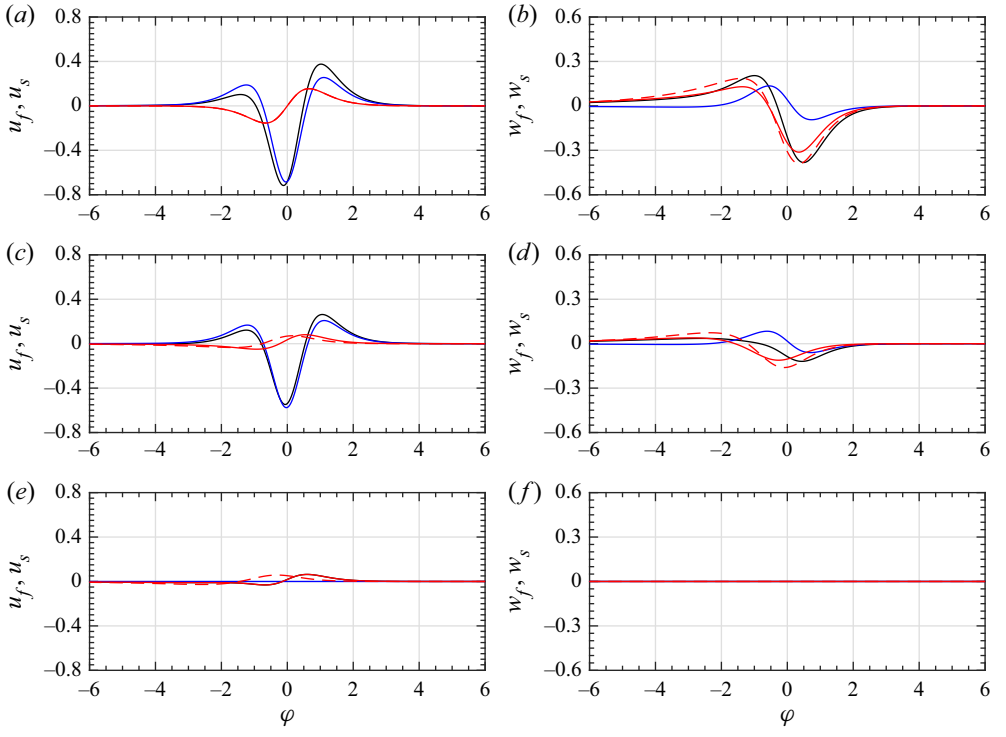

Figure 13. Time histories of solitary-wave-induced dimensionless velocity components at three different elevations, (*a*,*b*) $Z = 1$, (*c*,*d*) $Z = 0.5$ and (*e*,*f*) $Z = 0$, within an unsaturated poroelastic seabed. Black solid lines, the pore fluid velocity components; blue solid lines, the soil skeleton velocity components; red solid lines, the velocity difference of the pore fluid and soil skeleton calculated by the present solutions; and red dashed lines, the velocity difference of the pore fluid and soil skeleton calculated by Liu *et al.* (2007) for a rigid soil skeleton. The physical parameters used in the calculation are given in the caption of figure 11.

at three elevations inside the seabed, $Z = 1.0$, 0.5 and 0, respectively, are displayed. The moving coordinate, $\varphi = x - Ct$, is adopted for convenience. Under the present conditions, the diffusion depth of the pore pressure, $1/\alpha$, is 0.36. Below the diffusion depth, the vertical pressure gradient is small, and $p \to \beta p_b$. Therefore, the pore pressure at $Z = 0.5$ and $Z = 0$ starts to grow in parallel to the wave loading (see figure 15). Meanwhile, the diffusion time scale, α^2, decreases, when $G \to \infty$. Thus, compared with the solution of Liu *et al.* (2007), the present poroelastic solution starts to increase earlier and takes a longer time to reach the maximum value.

The contours of the pore pressure and the effective stresses are displayed in figure 16. The results also show that the normal effective stresses, τ_{xx} and τ_{zz}, have the same sign, while the shear stress has the opposite sign. As compared to those under a solitary wave, the bore-induced responses correspond to those during the acceleration phase of the solitary wave.

In figure 17, time histories of the velocity components for the pore fluid and soil skeleton at three different elevations are shown. The vertical profiles of these velocity components in the seabed at five different phases, $\varphi = -2, -1, 0, 1$ and 2, are plotted in figure 18. As shown in these figures, the horizontal velocity component for the pore fluid and soil skeleton in the seabed reverses its direction from negative to positive as φ increases. However, the vertical velocity component first decreases, then increases to zero. Relatively,

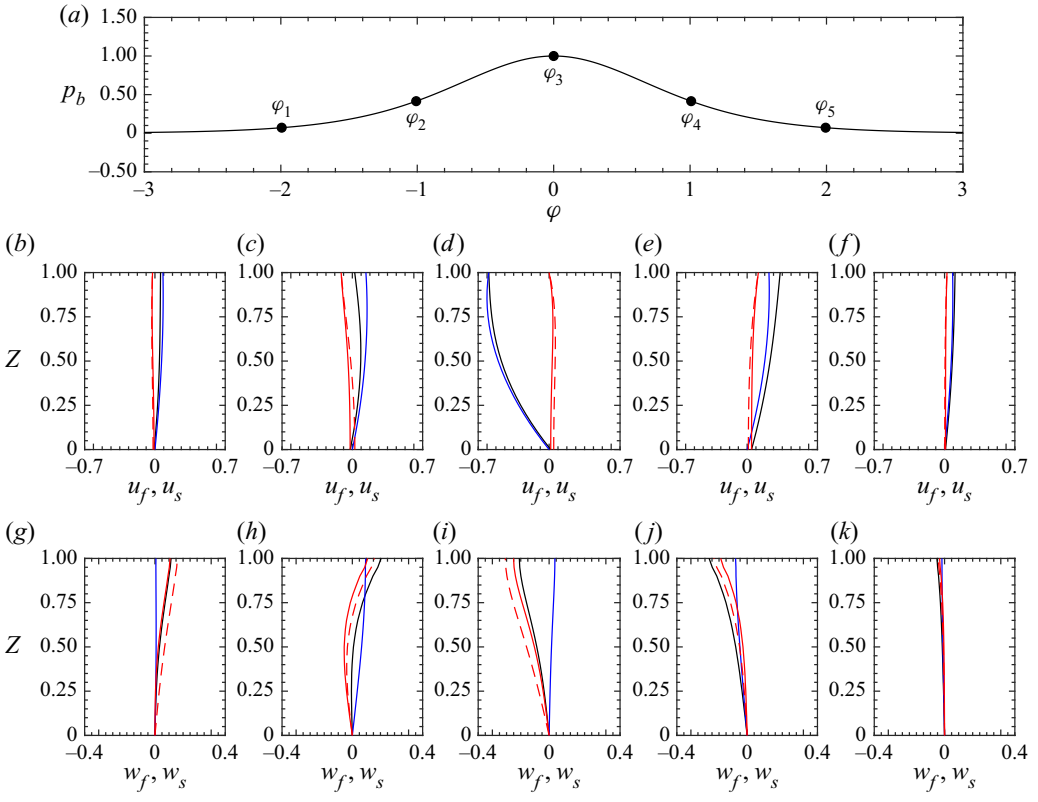

Figure 14. Vertical profiles of the dimensionless velocity components of the pore fluid, the soil skeleton and the seepage flow at five different phases: (*a*) the time history of the dynamic water pressure at the water–seabed interface; (*b–f*) the vertical profiles of the horizontal velocity components at $\varphi_1 = -2$, $\varphi_2 = -1$, $\varphi_3 = 0$, $\varphi_4 = 1$ and $\varphi_5 = 2$, respectively; and (*g–k*) the vertical profiles of the vertical velocity components at $\varphi_1 = -2$, $\varphi_2 = -1$, $\varphi_3 = 0$, $\varphi_4 = 1$ and $\varphi_5 = 2$, respectively. Black solid lines, the pore fluid velocity components; blue solid lines, the soil skeleton velocity components; red solid lines, the differences of the pore fluid and soil skeleton velocities calculated by the present solutions; and red dashed lines, the difference of the pore fluid and soil skeleton velocities calculated by Liu *et al.* (2007). The physical parameters used in the calculation are given in the caption of figure 11.

the vertical soil skeleton velocity components are small (see figure 17). The differences of the velocities of the pore fluid and the soil skeleton are displayed in these figures as well. Since the pore pressure speeds up to increase at first and then slows down to be a constant (see figure 15), the horizontal relative velocity component first increases, and then gradually decreases to zero inside the seabed. Correspondingly, the vertical relative velocity component behaves in the opposite manner. At the seabed bottom, the vertical relative velocity component is zero, as required by the condition of no vertical flow.

The comparisons of the present solution with the solution of Liu *et al.* (2007) show that the soil skeleton deformation has some influence on the damping rate and the phase shift of the seepage velocity under a bore. Under the bore front, the soil is compressed as shown in figure 16. The vertical velocity component of the soil skeleton is negative and damps with the increase of the soil depth, which prevents the fluid from flowing into the seabed. Thus, the difference of the vertical relative velocities of these two solutions decreases with increasing soil depth. The results also show that the difference of the relative velocities

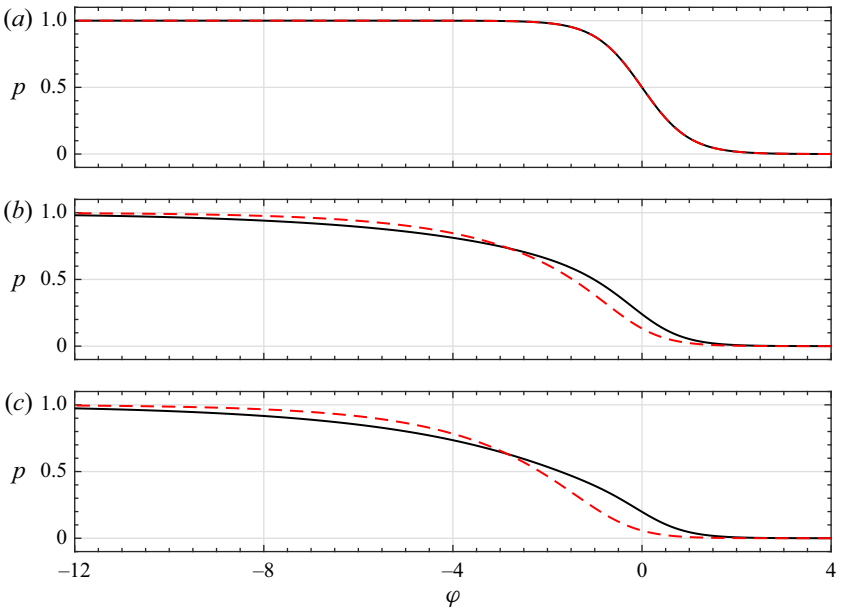

Figure 15. Time histories of the bore-induced dimensionless pore pressure at three different elevations inside the seabed: (*a*) $Z = 1$, (*b*) $Z = 0.5$ and (*c*) $Z = 0$.Black solid lines, the present solution; and red dashed lines, the solution of Liu *et al.* (2007). The physical parameters used in the calculation are given in the caption of figure 11.

of the present solution and the solution of Liu *et al.* (2007) increases with increasing soil depth in the horizontal direction.

6. Wave-induced shear failure potential inside the seabed

The wave-induced effective stresses can cause shear failure inside the seabed (Yamamoto 1977). Such kind of failure can produce horizontal movement of soil (Jeng 2003), which is an important driver for morphological changes and sediment transport. In this section, transient wave-induced shear failure potential inside the seabed is evaluated by the present theory. Based on the Mohr–Coulomb criterion, shear failure occurs when the stress angle, ϕ, in the seabed exceeds the internal friction angle of the soil, ϕ_c, namely (Yamamoto 1977)

$$\phi \geq \phi_c, \tag{6.1}$$

where ϕ_c depends on the soil type; for sand, ϕ_c is between 30° and 35° (Jeng 1997). Therefore, $\phi_c = 31°$ is used for analysis in the rest of the paper. Based on Yamamoto (1978), the stress angle, ϕ, can be expressed in terms of the wave-induced effective stresses, i.e. (3.18), (3.20) and (3.21), as

$$\phi = \arcsin\left(\frac{\sqrt{[(-\tau_{z0}/\kappa_3 - \tau_{zz}) - (-\tau_{x0}/\kappa_3 - \tau_{xx})]^2 + 4\tau_{xz}^2}}{(-\tau_{z0}/\kappa_3 - \tau_{zz}) + (-\tau_{x0}/\kappa_3 - \tau_{xx})}\right), \tag{6.2}$$

in which τ_{z0} and τ_{x0} are the effective stresses at the quiescent state, and κ_3 is the normalized wave amplitude, i.e.

$$\kappa_3 = a_0'/d'. \tag{6.3}$$

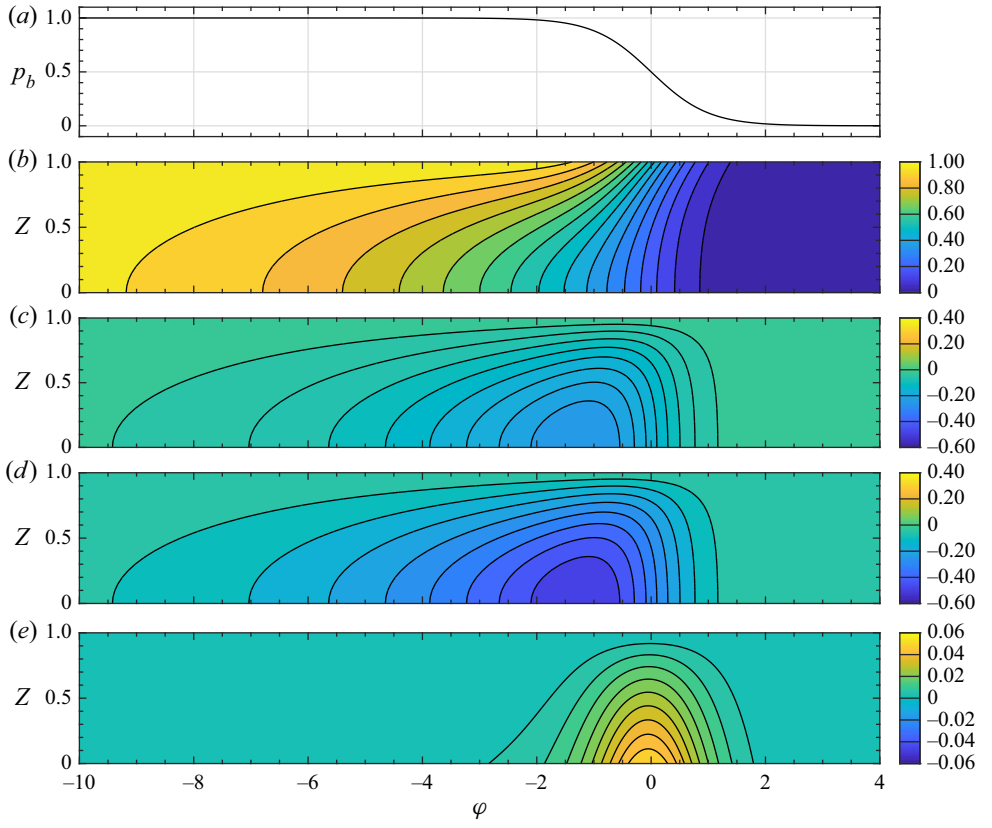

Figure 16. Contours of the pore pressure and effective stresses under a bore: (*a*) the time history of the dynamic water pressure at the water–seabed interface; (*b*) contours of the pore pressure p; (*c*) contours of the horizontal effective stress τ_{xx}; (*d*) contours of the vertical effective stress τ_{zz}; and (*e*) contours of the shear stress τ_{xz}. The physical parameters used in the calculation are given in the caption of figure 11.

Since the pressure field begins from the quiescent state, the soil is assumed to be consolidated under the buoyant weight, and therefore τ_{z0} and τ_{x0} normalized by $\rho_f g d'$ can be estimated by (Madsen 1978; Yamamoto 1978)

$$\tau_{z0} = \frac{1}{1-2\tilde{\nu}}\tau_{x0} = -(1-n)(\psi-1)(1-Z), \tag{6.4}$$

in which ψ denotes the density ratio between soil particles and pore fluid. In this paper $\psi = 2.63$ is used for analysis.

Based on (3.20) and (6.4), equation (6.2) can be further expressed as

$$\phi = \arcsin\left(\frac{\sqrt{\tilde{\nu}^2(\tau_{z0}/\kappa_3+\tau_{zz})^2+\tau_{xz}^2}}{(1-\tilde{\nu})(-\tau_{z0}/\kappa_3-\tau_{zz})}\right). \tag{6.5}$$

The equation above indicates that, at the quiescent state, the stress angle inside the seabed is a constant, i.e. $\phi = \arcsin(\tilde{\nu}/(1-\tilde{\nu}))$. An an example, consider the following wave conditions and soil properties: $h' = 40$ m, $T' = 12.5$ s, $a_0' = 2.5$ m, $d' = 20$ m, $k_s = 2.04\times10^{-11}$ m^2, $G = 10^7$ Pa, $K = 1.9\times10^7$ Pa ($S_r = 0.98$), $n = 0.3$, $v = 0.33$

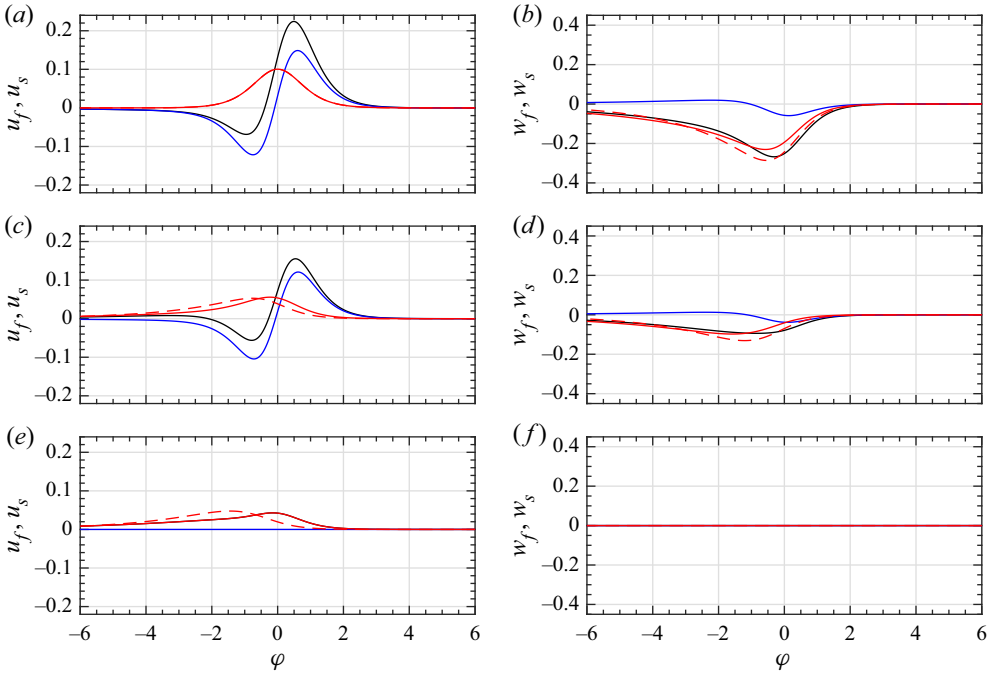

Figure 17. Time histories of the bore-induced dimensionless velocity components for the pore fluid and soil skeleton at three different elevations: (*a*,*b*) $Z = 1$, (*c*,*d*) $Z = 0.5$ and (*e*,*f*) $Z = 0$. Black solid lines, the pore fluid velocity components; blue solid lines, the soil skeleton velocity components; red solid lines, the relative velocity between pore fluid and soil skeleton calculated by the present solutions; and red dashed lines, the relative velocity between pore fluid and soil skeleton calculated by Liu *et al.* (2007). The physical parameters used in the calculation are given in the caption of figure 11.

and $\psi = 2.4$. Under these conditions, the maximum stress angle is 53° and is located at the water–seabed interface. The normalized shear failure depth is 0.03, with $\phi_c = 32°$, which agrees well with the numerical results calculated by Lin & Li (2001).

6.1. *Transient wave-induced shear failure potential in the seabed*

Using the experimental conditions listed in table 1, the stress angle inside the seabed given by Anderson *et al.* (2017) can be calculated and is shown in figure 19. The stress angle increases during the acceleration phase and has larger values near the bottom of the seabed. The maximum stress angle in the entire wave cycle, ϕ_{max}, is 29.8°, which is smaller than the internal friction angle of the prescribed soil properties ($\phi_c = 30.1°$), suggesting that shear failure is unlikely to occur inside the seabed for this experimental set-up.

Under the linear wave conditions and soil properties presented in § 5, the stress angles within the seabed are calculated from (6.5). Figure 20 shows the contour map of the stress angle during the second and third wave periods. Owing to the wave-induced effective stresses, the stress angles inside the seabed increase in both the deceleration and acceleration phases. Since the wave-induced effective vertical normal stress is positive (tension) in the deceleration phase and negative (compression) in the acceleration phase (see figure 8), the effective weight of the soil decreases in the deceleration phase and increases in the acceleration phase. Recall that the wave-induced effective shear stress

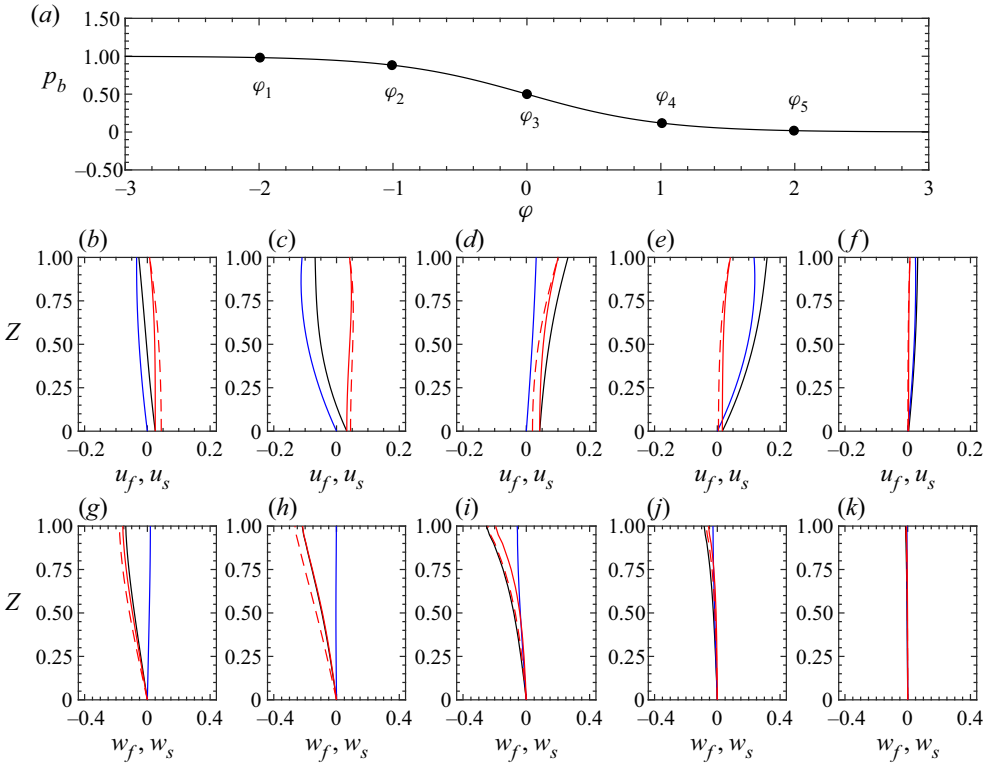

Figure 18. Vertical profiles of the dimensionless velocity components of the pore fluid and the soil skeleton in the seabed at five different phases: (*a*) the time history of the dynamic water pressure at the water–seabed interface; (*b–f*) the vertical profiles of the horizontal velocity components at $\varphi_1 = -2$, $\varphi_2 = -1$, $\varphi_3 = 0$, $\varphi_4 = 1$ and $\varphi_5 = 2$, respectively; and (*g–k*) the vertical profiles of the vertical velocity components at $\varphi_1 = -2$, $\varphi_2 = -1$, $\varphi_3 = 0$, $\varphi_4 = 1$ and $\varphi_5 = 2$, respectively. Black solid lines, the pore fluid velocity components; blue solid lines, the soil skeleton velocity components; red solid lines, the relative velocity between pore fluid and soil skeleton calculated by the present solutions; and red dashed lines, the relative velocity between pore fluid and soil skeleton calculated by Liu *et al.* (2007). The physical parameters used in the calculation are given in the caption of figure 11.

is symmetric, and therefore the stress angle increases more in the deceleration phase. The results show that the maximum stress angle under the linear wave is 31.6°, which is around the critical value, 31°. As shown in figure 20, shear failure may occur near the water–seabed interface in the deceleration phase, which is consistent with Ren *et al.* (2020).

Combining the wave-induced effective stresses calculated in § 5 with the effective stresses at the quiescent state, the stress angle under the solitary wave can be obtained, which is shown in figure 21(*b*). The stress angle decreases towards the bottom of the soil bed and reaches its maximum in the deceleration phase at the water–seabed interface. Under the present solitary-wave conditions (i.e. $a_0'/h' = 0.2$ and $h' = 30$ m) and soil properties, the maximum stress angle is estimated as 20.7°, and it is not large enough to cause shear failure, which is $\phi_c = 31°$. However, if a_0'/h' increases to 0.4, as discussed in Packwood & Peregrine (1980) with the same seabed properties, the maximum of ϕ increases drastically to 90°. Clearly, the criterion of (6.1) will be satisfied. Figure 22 shows the contour map of the stress angle for this large solitary wave. The results indicate

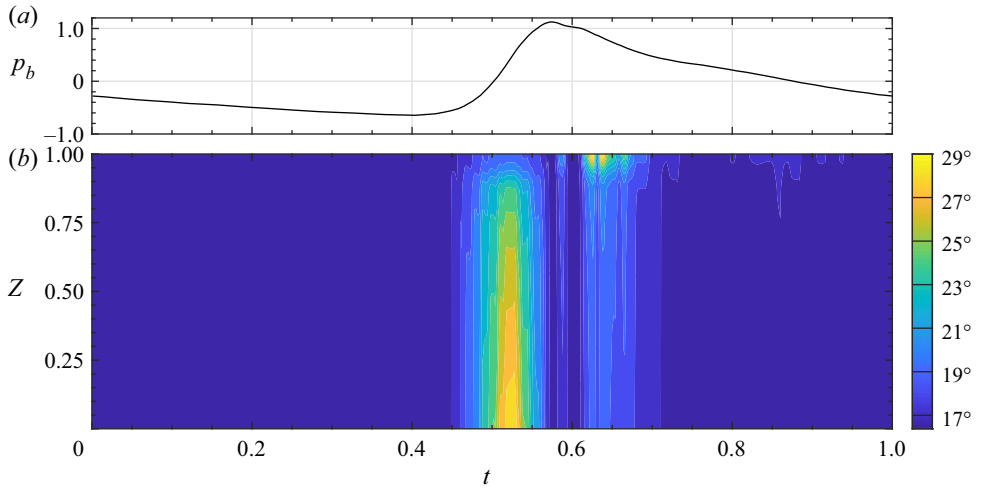

Figure 19. (*a*) Time history of the phase-averaged dynamic water pressure at the water–seabed interface measured by Anderson *et al.* (2017). (*b*) The contour map of the stress angle inside the seabed. The stress angle achieves its maximum, 29.8°, at the seabed bottom when $t = 0.525$. The physical parameters are given in table 1.

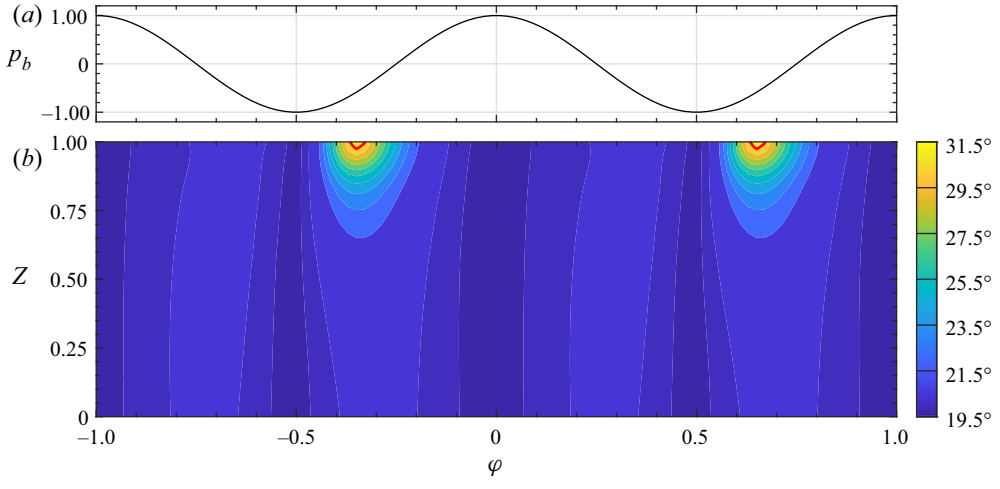

Figure 20. (*a*) The time history of the dynamic water pressure at the water–seabed interface under a linear wave with $T' = 15$ s, $h' = 30$ m and $a_0'/h' = 0.10$. (*b*) The colour map of the stress angle inside the seabed during linear wave propagation. The stress angle achieves the maximum, 31.6°, at the water–seabed interface in the deceleration phase, and the red line indicates the contour of $\phi = \phi_c$. The physical parameters used in the calculation are given in the caption of figure 7.

that the shear failure depth reaches up to 20 % of the seabed thickness. Recall that solitary-wave-induced effective vertical normal stress is also negative (compression) in the acceleration phase and positive (tension) in the deceleration phase, and therefore shear failure is more likely to occur in the deceleration phase. As suggested by Yamamoto (1978), the total effective stresses will vanish, and the sand will be liquefied, when the stress angle reaches 90°. As shown in figure 22, under such a large solitary wave, momentary liquefaction may occur near the water–seabed interface as well, and it starts after the

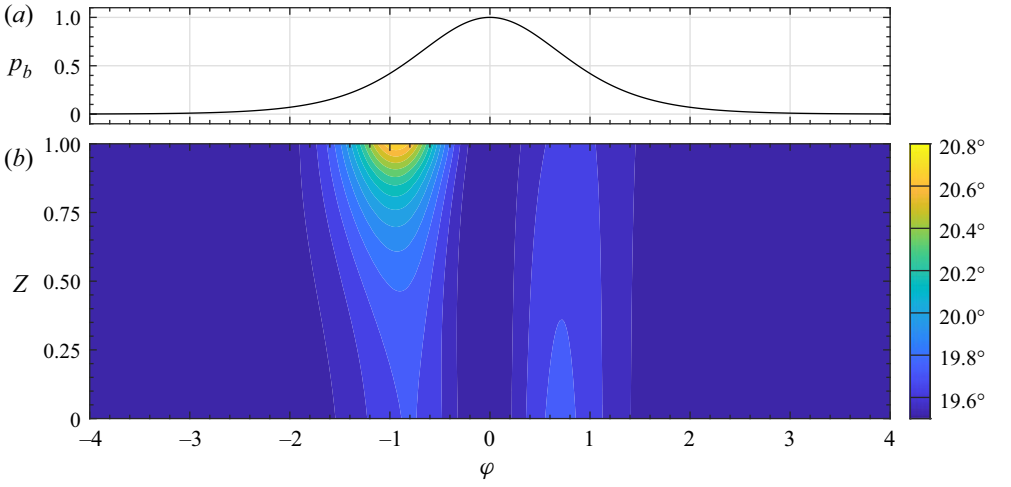

Figure 21. (*a*) The time history of the dynamic water pressure at the water–seabed interface under a solitary wave with $a_0'/h' = 0.2$ and $h' = 30$ m. (*b*) The colour map of the stress angle inside the seabed under a solitary wave. The stress angle achieves the maximum, 20.7°, at the water–seabed interface when $\varphi = -0.94$. The physical parameters used in the calculation are given in the caption of figure 11.

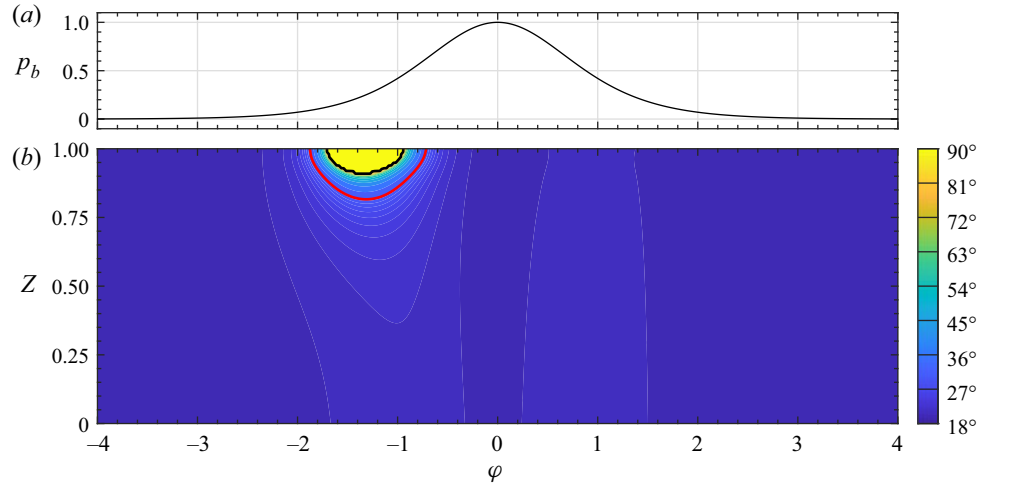

Figure 22. (*a*) The time history of the dynamic water pressure at the water–seabed interface under a solitary wave with $a_0'/h' = 0.4$ and $h' = 30$ m. (*b*) The colour map of the stress angle inside the seabed. The red line indicates the contour of $\phi = \phi_c$, and the black line indicates the contour of $\phi = 90°$. The other parameters used in the calculation are consistent with those given in the caption of figure 11.

beginning of shear failure and ends before the end of shear failure. Note that the poroelastic theory is no longer valid once shear failure occurs. To investigate the liquefaction potential and related processes within the seabed, a poroelastoplastic model is further required (Young *et al.* 2009).

Using the wave conditions and seabed properties presented in § 5, the stress angles under the bore are calculated and displayed in figure 23. The stress angle increases from the water–seabed interface towards the bottom of the seabed. The maximum value, 19.98°, appears at the bottom of the seabed when $\varphi = 0.04$. Clearly, shear failure does not occur

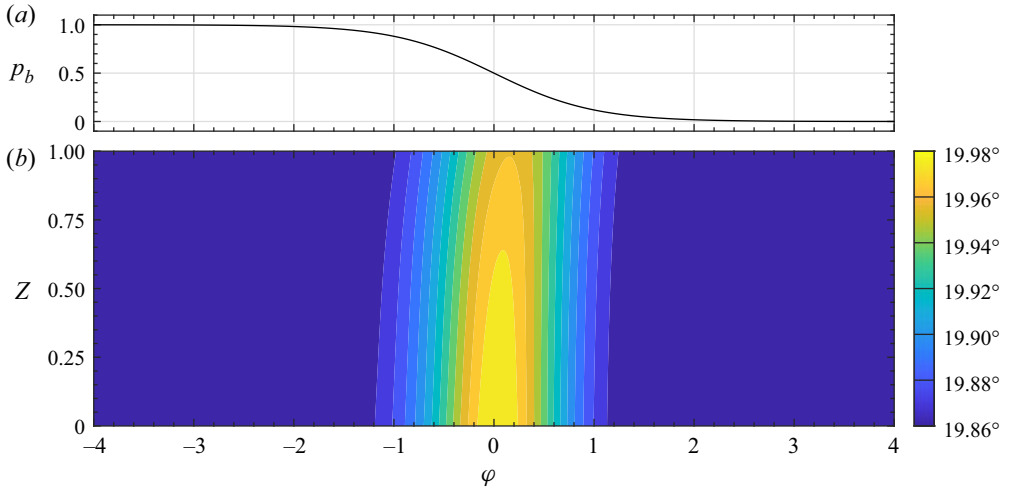

Figure 23. (*a*) History of the dynamic water pressure at the water–seabed interface under a bore. (*b*) Contours of the stress angle inside the seabed under a bore. The stress angle reaches the maximum 19.98° at the bottom of the seabed when $\varphi = 0.04$. The physical parameters used in the calculation are given in the caption of figure 11.

within the seabed for this case, since the internal friction angle of the soil is 31°. Note that, under a bore, the pore pressure is always in the acceleration phase and the effective normal stress is always in compression, which create a less favourable condition for shear failure. However, the effective shear stress also contributes to the increase of stress angle, i.e. see (6.4). Thus, the potential of shear failure will increase if the bore strength is increased. For example, if a_0'/h' is increased to 1, which is most likely a breaking bore, the maximum stress angle increases to 24.9°, which is still not large enough to cause shear failure. However, if a_0'/h' is further increased to 2, the maximum stress angle increases to 36.3°, and shear failure occurs near the bottom of the seabed. Note that such a violent (turbulent) bore could occur in extreme conditions, such as tsunamis; however, the frictional stress on the water–seabed interface becomes significant and needs to be considered. This is beyond the scope of the present study.

6.2. *Effects of soil properties on shear failure*

The analytical solutions for the wave-induced effective stresses (i.e. (3.18), (3.20) and (3.21)) depend on the soil properties, such as the degree of saturation S_r, the shear modulus G and the permeability k_s, suggesting that the shear failure potential of the seabed is affected by the soil properties as well. In this section, as an illustration, the effects of these three parameters (S_r, G and k_s) on the shear failure are investigated under solitary waves with $a_0'/h' = 0.4$ and $h' = 30$ m.

First, the effects of the degree of saturation, S_r, on shear failure are investigated for a highly saturated seabed with S_r between 0.94 and 0.998 (Sumer 2014). The corresponding bulk modulus of elasticity of the pore fluid, K, varies from 4.9×10^6 Pa to 1.38×10^8 Pa. The other soil parameters remain the same as those presented in § 5. Using (6.5), the stress angle ϕ inside the seabed can be calculated. For a specified elevation Z, shear failure does not occur if the maximum of ϕ, denoted by $\phi_{max}(S_r, Z)$, is smaller than the critical value ϕ_c, namely $\phi_{max}(S_r, Z) < \phi_c$. Therefore, the values of $\phi_{max}(S_r, Z)$ in the parameter space

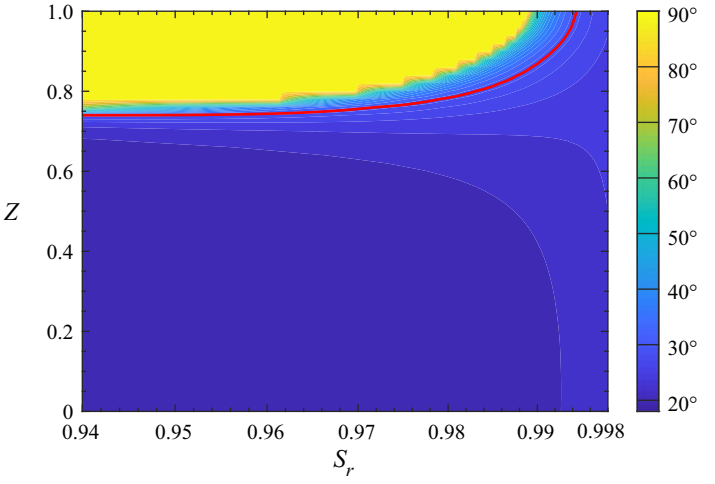

Figure 24. The contour map of the maximum stress angle $\phi_{max}(S_r, Z)$ induced by a solitary wave with $a_0'/h' = 0.4$ and $h' = 30$ m (the red line indicates the contour of $\phi_{max}(S_r, Z) = \phi_c$). Shear failure occurs when $S_r \leq 0.9943$. The physical parameters used in the calculation are given in the caption of figure 11.

$0.94 < S_r < 0.998$ and $0 < Z < 1$ are numerically calculated and displayed in figure 24. In figure 24, the red line indicates the contour of $\phi_{max}(S_r, Z) = \phi_c$. The region below the red line is called the stable zone and the region above is called the shear failure zone in this paper.

As shown in figure 24, $\phi_{max}(S_r, Z)$ is sensitive to the change of saturation. Shear failure occurs near the water–seabed interface when the saturation degree S_r is smaller than 0.9943, and the shear failure depth decreases gradually when S_r increases from 0.94 to 0.9943. For a seabed with large saturation degree, the ratio between G and K measured by $\tilde{G}$ is relatively small; for example, when $S_r = 0.998$, $\tilde{G} = 0.065$. Accordingly, the dimensionless parameter β is relatively large, indicating that the wave-induced effective stresses are weak inside the seabed. Thus, it is difficult for shear failure to happen in this situation. When S_r decreases, the diffusion depth of the wave-induced pressure decreases as well and the effective stresses increase rapidly in the diffusion region. Therefore, the maximum stress angle quickly damps to a small value with increasing soil depth.

Besides the shear failure potential, information on the initiation and duration of shear failure are also important. Figure 25 shows the interface of the shear failure zone and the stable zone under four different degrees of saturation degree, i.e. $S_r = 0.96, 0.98, 0.99$ and 0.993. Under the solitary wave, shear failure starts earlier and ends later with decreasing degree of saturation.

For dense sand, the shear modulus of the seabed, G, is of the order of magnitude of $O(10^8$ Pa), but it reduces to $O(10^6$ Pa) for loose sand (Yamamoto 1978; Zhai *et al.* 2018). The effects of shear modulus on shear failure are studied for 2×10^6 Pa $< G < 4.4 \times 10^8$ Pa. Using the soil properties presented in § 5, the dimensionless parameter $\tilde{G}$ varies from 0.045 to 10. By numerical integration, the maximum stress angle, $\phi_{max}(\tilde{G}, Z)$, can be calculated and is displayed in figure 26.

In figure 26, the red line denotes the contour of $\phi_{max}(\tilde{G}, Z) = \phi_c$. Shear failure occurs when $\tilde{G}$ is larger than 0.068. Near the water–seabed interface, the maximum stress angle

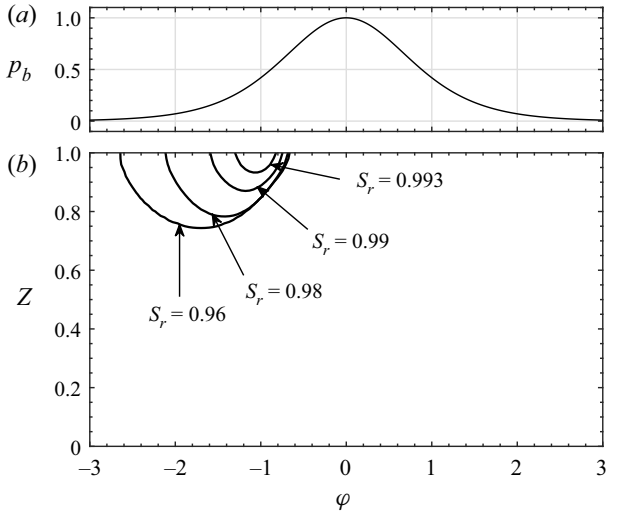

Figure 25. (*a*) The time history of the dynamic water pressure at the water–seabed interface under a solitary wave with $a_0'/h' = 0.4$ and $h' = 30$ m. (*b*) The interface between the shear failure zone and the stable zone under the conditions of $S_r = 0.96$, 0.98, 0.99 and 0.993. The parameters used in the calculation are given in the caption of figure 11.

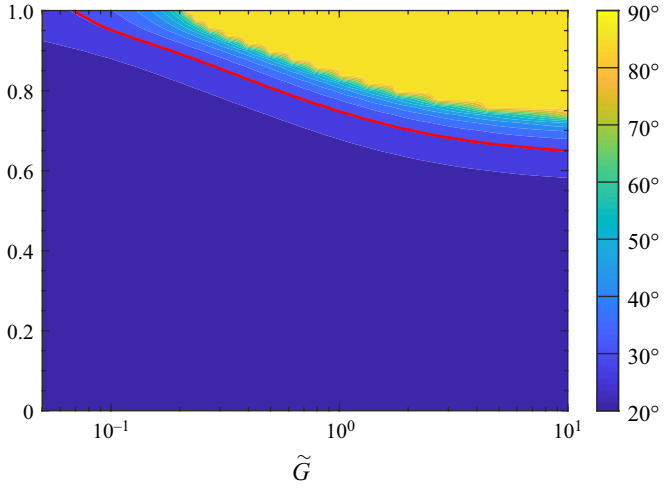

Figure 26. The contour map of the maximum stress angle, $\phi_{max}(\tilde{G}, Z)$, induced by a solitary wave with $a_0'/h' = 0.4$ and $h' = 30$ m. The red line indicates the contour of $\phi_{max}(\tilde{G}, Z) = \phi_c$, and shear failure occurs when $\tilde{G} \geq 0.068$. In the calculation, the shear modulus varies between 2×10^6 Pa and 4.4×10^8 Pa, and the other physical parameters used in the calculation are given in the caption of figure 11.

increases rapidly with increasing $\tilde{G}$. For a loose seabed, $\tilde{G}$ is small, and the dimensionless parameter β approaches 1. Similar to the scenario of a large degree of saturation, the wave-induced effective vertical normal stress τ_{zz} is small. Physically, this means that most of the wave loading is balanced by the pore fluid, as the soil skeleton is easier to compress than the pore fluid. Hence shear failure is unlikely to occur inside the seabed in this case. However, for dense seabed with relatively large $\tilde{G}$, the dimensionless parameter β becomes

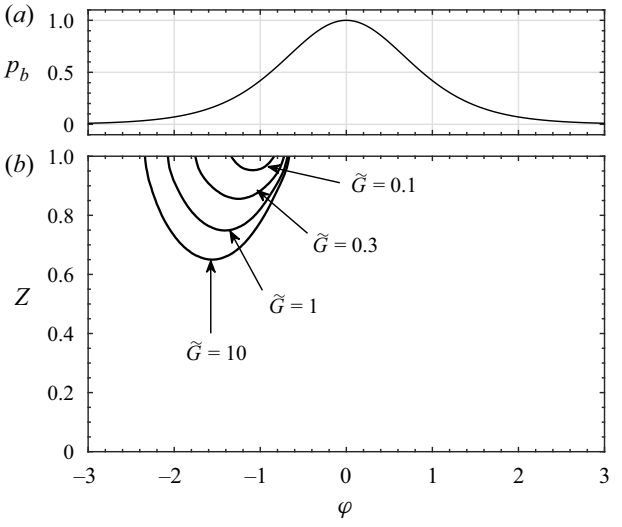

Figure 27. (*a*) The time history of the dynamic water pressure at the water–seabed interface under a solitary wave with $a_0'/h' = 0.4$ and $h' = 30$ m (*b*) The interface between the shear failure zone and the stable zone under the conditions of $\tilde{G} = 0.1$, 0.3, 1.0 and 10. The other parameters used in the calculation are given in the caption of figure 11.

close to 0. For example, when $\tilde{G} = 10$, then $\beta = 0.02$. Meanwhile, the dimensionless parameter α, which can be viewed as the inverse of the diffusion distance for the pore pressure, is insensitive to the change of shear modulus when $\tilde{G}$ is relatively large. For example, $\alpha = 2.72$ when $\tilde{G} = 5$, and $\alpha = 2.69$ when $\tilde{G} = 10$. Based on (3.18), τ_{zz} varies over a wide range in this scenario, and the wave-induced tension stress in the deceleration phase is relatively large. Consequently, the shear failure potential increases.

Figure 27 further shows the interface between the shear failure zone and the stable zone under four different shear modulus conditions, i.e. $\tilde{G} = 0.1$, 0.3, 1.0 and 10. Shear failure starts earlier and ends later with increasing shear modulus.

Since the soil permeability k_s is of the order of magnitude of $O(10^{-11}\ \mathrm{m}^2)$ for fine sandy seabed and $O(10^{-9}\ \mathrm{m}^2)$ for coarse sandy seabed (Hsu & Jeng 1994), the effects of the soil permeability on shear failure are studied for $10^{-11}\ \mathrm{m}^2 < k_s < 10^{-9}\ \mathrm{m}^2$. The corresponding dimensionless parameter κ_2^2 varies from 2.1×10^{-4} to 2.1×10^{-2}. The contour map of the maximum stress angle $\phi_{max}(\kappa_2^2, Z)$ is produced and displayed in figure 28. In the figure, the red line represents the contour of $\phi_{max}(\kappa_2^2, Z) = \phi_c$, separating the shear failure zone and the stable zone. As shown in figure 28, shear failure always occurs near the water–seabed interface. Meanwhile, the shear failure depth is affected by the soil permeability, because the diffusion distance of p measured by $1/\alpha$ increases with increasing k_s.

Figure 29 further shows the interface between the shear failure zone and stable zone under three different permeability conditions, $\kappa_2^2 = 2 \times 10^{-3}$, 7×10^{-3} and 2×10^{-2}. Shear failure starts early and lasts for a short time when κ_2^2 is relatively large. This is because it is more difficult for the pore fluid to drain out to dissipate the wave-induced pore pressure for the seabed with small permeability.

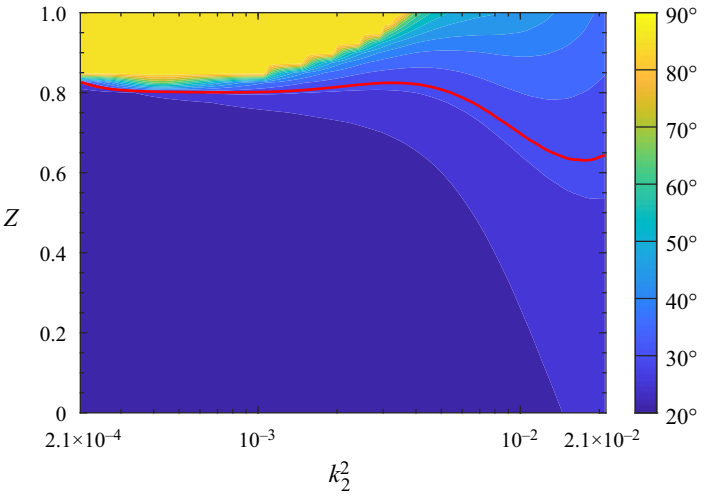

Figure 28. The contour map of the maximum stress angle, $\phi_{max}(\kappa_2^2, Z)$, induced by a solitary wave with $a_0'/h' = 0.4$ and $h' = 30$ m; the red line indicates the contour of $\phi_{\max}(\kappa_2^2, Z) = \phi_c$. In the calculation, the soil permeability varies from 10^{-11} m^2 to 10^{-9} m^2, and the other physical parameters used in the calculation are given in the caption of figure 11.

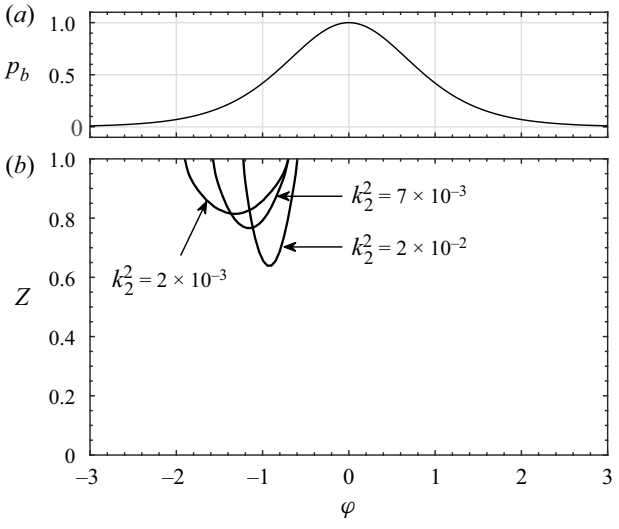

Figure 29. (*a*) The time history of the dynamic water pressure at the water–seabed interface under a solitary wave with $a_0'/h' = 0.4$ and $h' = 30$ m. (*b*) The interface between the shear failure zone and the stable zone under soil permeability conditions of $\kappa_2^2 = 2 \times 10^{-3}$, 7×10^{-3} and 2×10^{-2}. The parameters used in the calculation are given in the caption of figure 11.

7. Concluding remarks

In this study, we presented analytical solutions for transient wave-induced soil responses within a poroelastic seabed of finite thickness. In the framework of consolidation theory, the soil skeleton was treated as a poroelastic medium and the pore fluid was assumed to be unsaturated. Since the effective bulk modulus of elasticity of the pore fluid varies with the degree of saturation, and can be of the same order of magnitude as the shear modulus

of the soil, the compression of both the pore fluid and soil skeleton were considered for the dynamic and kinematic responses in the seabed. However, the vertical thickness of the seabed was assumed to be much smaller than the wavelengths of the ocean waves and the shear waves. As a result, the present theory is applicable for a general transient wave loading, periodic or non-periodic.

To validate the present poroelastic theory, we compared the analytical solutions for the pore pressure and its gradients with two sets of laboratory measurements. The comparisons of the theoretical results and experimental data demonstrate that the assumptions made in this study are reasonable, and the present solutions are reliable in predicting the wave-induced pore pressure and its gradients within a sandy bed of finite thickness. Using the present poroelastic theory, the dynamic and kinematic responses inside a sandy seabed under transient wave loadings, including a linear periodic wave train, a solitary wave and a bore, were investigated in detail and were compared with the previous study of Liu *et al.* (2007). The results showed that the soil deformation is important to transient wave-induced soil responses when the effective bulk modulus of elasticity of the pore fluid, K, is close to the shear modulus of the soil, G.

As an application, the present theory was used to investigate seabed instability. The shear failure potential under transient waves was studied. The results indicated that shear failure can be caused inside a sandy seabed by transient waves during the deceleration phase. The analysis also demonstrated that the shear failure potential and duration are highly dependent on the soil properties, such as the saturation degree, shear modulus and permeability.

Acknowledgements. Dr B. Liu is acknowledged for providing information on the one-dimensional experiments and discussions about the values of the shear modulus used in this paper.

Funding. L.L.T. is funded by the National Postdoctoral Program for Innovative Talents of China (BX20190105), the Major International Joint Research Project POW3M (51920105013), the Fundamental Research Funds for the Central Universities (B200202062) and the National Natural Science Foundation of China (52101309). P.L.-F.L. would like to acknowledge support from the Faculty of Engineering at the National University of Singapore through an initiative grant. This research was also supported in part by the Yushan Fellow Program, Ministry of Education, Taiwan.

Declaration of interests. The authors report no conflict of interest.

Author ORCIDs.
Linlong Tong https://orcid.org/0000-0003-3195-6833;
Philip L.-F. Liu https://orcid.org/0000-0002-2170-5507.

Author contributions. L.L.T.: analytical analysis; data analysis; writing. P.L.-F.L.: conceptualization; writing – review and editing; supervision; project administration.

Appendix A. The continuity equation for the soil skeleton

In this appendix, we present the derivation of the continuity equation for the soil skeleton, (2.3). According to Yamamoto *et al.* (1978) and (2.1), the dimensionless continuity equation for the soil skeleton is given by

$$\frac{\kappa_2^2}{\kappa_1^2}\left(\kappa_1^2\frac{\partial^2 p}{\partial x^2}+\frac{\partial^2 p}{\partial Z^2}\right)=n\frac{G}{K}\frac{\partial p}{\partial t}+\frac{\partial \epsilon}{\partial t}. \tag{A1}$$

In the above equation, κ_2 is given by (2.4), and ϵ is the dimensionless volume strain of the soil skeleton, which is defined by (Yamamoto *et al.* 1978)

$$\epsilon = \kappa_1^2 \frac{\partial U_s}{\partial x} + \frac{\partial W_s}{\partial Z}, \tag{A2}$$

with U_s and W_s denoting the dimensionless displacements of the soil skeleton in the horizontal and vertical directions, respectively. The left-hand side of (A1) is the discharge volume of the pore fluid, the first term on the right-hand side of (A1) denotes the compression volume of the pore fluid, and the last term of (A1) represents the compression volume of the soil skeleton. The relations between the velocity and displacement of the soil skeleton can be expressed as

$$u_s = \frac{\partial U_s}{\partial t} + \kappa_1^2 \gamma u_s \frac{\partial U_s}{\partial x} + \gamma w_s \frac{\partial U_s}{\partial Z} \quad \text{and} \quad w_s = \frac{\partial W_s}{\partial t} + \kappa_1^2 \gamma u_s \frac{\partial W_s}{\partial x} + \gamma w_s \frac{\partial W_s}{\partial Z}. \tag{A3a,b}$$

In coastal regions, γ is a typical small parameter; for example, $\gamma = 0.001$ when $a_0' = 1$ m and $G = 10^7$ Pa. Therefore, substituting (A2) and (A3*a*,*b*) into (A1), the continuity equation for the soil skeleton can be simplified as

$$\frac{\kappa_2^2}{\kappa_1^2} \frac{\partial^2 p}{\partial Z^2} - \frac{\partial w_s}{\partial Z} + \kappa_1^2 \left(\frac{\kappa_2^2}{\kappa_1^2} \frac{\partial^2 p}{\partial x^2} - \frac{\partial u_s}{\partial x} \right) = n \frac{G}{K} \frac{\partial p}{\partial t}. \tag{A4}$$

The above equation is consistent with the continuity equation used in Mei & Foda (1981).

References

Abdolali, A., Kadri, U. & Kirby, J. 2019 Effect of water compressibility, sea-floor elasticity, and field gravitational potential on tsunami phase speed. *Sci. Rep.* **9** (1), 16874.

Anderson, D., Cox, D., Mieras, R., Puleo, J.A. & Hsu, T.-J. 2017 Observations of wave-induced pore pressure gradients and bed level response on a surf zone sandbar. *J. Geophys. Res.* **122**, 5169–5193.

Baumgarten, A.S. & Kamrin, K. 2019 A general fluid–sediment mixture model and constitutive theory validated in many flow regimes. *J. Fluid Mech.* **861**, 721–764.

Bear, J. 1972 *Dynamics of Fluids in Porous Media*. Dover.

Biot, M.A. 1941 General theory of three-dimensional consolidation. *J. Appl. Phys.* **26**, 155–164.

Body, G.L. & Ehrenmark, U.T. 1998 Reflection of gravity waves by a steep beach with a porous bed. *J. Fluid Mech.* **359**, 265–280.

Chan, I.C. & Liu, P.L.-F. 2012 On the runup of long waves on a plane beach. *J. Geophys. Res.* **117**, 1–17.

Chanson, H. 2009 Current knowledge in hydraulic jumps and related phenomena. A survey of experimental results. *Eur. J. Mech.* B/*Fluids* **28**, 191–210.

Dean, R.G. & Dalrymple, R.A. 1991 Water wave mechanics for engineers and scientists. In *Advanced Series on Ocean Engineering* (ed. P.L.-F. Liu). World Scientific.

Hsu, C.J., Chen, Y.Y. & Tsai, C.C. 2019 Wave-induced seabed response in shallow water. *Appl. Ocean Res.* **89**, 211–223.

Hsu, J.R.C. & Jeng, D.S. 1994 Wave-induced soil response in an unsaturated anisotropic seabed of finite thickness. *Intl J. Numer. Anal. Meth. Geomech.* **18**, 785–807.

Jeng, D.S. 1997 Wave-induced seabed instability in front of a breakwater. *Ocean Engng* **24**, 887–917.

Jeng, D.S. 2003 Wave-induced sea floor dynamics. *Appl. Mech. Rev.* **56**, 407–429.

Jeng, D.S. & Rahman, M. 2000 Effective stresses in a porous seabed of finite thickness: inertia effects. *Can. Geotech. J.* **37**, 1383–1392.

Jeng, D.S., Ye, J.H., Zhang, J.S. & Liu, P.L.-F. 2013 An integrated model for the wave-induced seabed response around marine structures: model verifications and applications. *Coastal Engng* **72**, 1–19.

Jia, Y.G, Tian, Z., Shi, X., Liu, J.P., Chen, J., Liu, X., Ye, R., Ren, Z. & Tian, J. 2019 Deep-sea sediment resuspension by internal solitary waves in the northern South China Sea. *Sci. Rep.* **9**, 12137.

KIM, Y., MIERAS, R.S., CHENG, Z., ANDERSON, D., HSU, T.-J., PULEO, J.A. & COX, D. 2019 A numerical study of sheet flow driven by velocity and acceleration skewed near-breaking waves on a sandbar using SedWaveFoam. *Coastal Engng* **152**, 103526.

KNOWLES, J. & YEH, H. 2018 On shoaling of solitary waves. *J. Fluid Mech.* **848**, 1073–1097.

LIN, M. & LI, J.C. 2001 Effects of surface waves and marine soil parameters on seabed instability. *Appl. Math. Mech.* **22**, 904–916.

LIU, B. & JENG, D.S. 2013 Laboratory study for pore pressure in sandy bed under wave loading. In *Proceedings of the 23th International Offshore and Polar Engineering Conference*, pp. 1432–1437. International Society of Offshore and Polar Engineers.

LIU, B., JENG, D.S., YE, G.L. & YANG, B. 2015 Laboratory study for pore pressures in sandy deposit under wave loading. *Ocean Engng* **106**, 207–219.

LIU, P.L.-F. 1973 Damping of water waves over porous bed. *J. Hydraul. Div. ASCE* **99**, 2263–2271.

LIU, P.L.-F., DAVIS, M.H. & DOWNING, S. 1996 Wave-induced boundary layer flows above and in a permeable bed. *J. Fluid Mech.* **325**, 195–218.

LIU, P.L.-F., PARK, Y.S. & LARA, J.L. 2007 Long-wave-induced flows in an unsaturated permeable seabed. *J. Fluid Mech.* **586**, 323–345.

MADSEN, O.S. 1978 Wave-induced pore pressures and effective stresses in a porous bed. *Géotecnique* **28**, 377–393.

MEI, C.C. & FODA, M.A. 1981 Wave-induced responses in a fluid-filled poro-elastic solid with a free surface – a boundary layer theory. *Geophys. J. R. Astron. Soc.* **66**, 597–631.

MERXHANI, A. & LIANG, D.F. 2012 Investigation of the poro-elastic response of seabed to solitary waves. In *Proceedings of the 22nd International Offshore and Polar Engineering Conference*, pp. 101–108. International Society of Offshore and Polar Engineers.

MEYER, V., LANGFORD, T. & WHITE, D.J. 2016 Physical modelling of pipe embedment and equalisation in clay. *Géotecnique* **66**, 602–609.

MIERAS, R.S., PULEO, J.A., ANDERSON, D., COX, D.T. & HSU, T.J. 2017 Large-scale experimental observations of sheet flow on a sandbar under skewed-asymmetric waves. *J. Geophys. Res.* **122**, 5022–5045.

MOSHAGEN, H. & TØRUM, A. 1975 Wave induced pressures in permeable seabeds. *J. Waterways Harbors Coast. Engng. Div. ASCE* **101**, 49–57.

PACKWOOD, A.R. & PEREGRINE, D.H. 1980 Loss of water wave energy due to percolation in a permeable sea bottom. *Coastal Engng* **3**, 221–242.

PUJARA, N., LIU, P.L.-F. & YEH, H. 2015 The swash of solitary waves on a plane beach: flow evolution, bed shear stress and run-up. *J. Fluid Mech.* **779**, 556–597.

PUTNAM, J.A. 1949 Loss of wave energy due to percolation in a permeable bottom. *Trans. Am. Geophys. Union* **30**, 349–355.

QI, W.G., LI, C.F., JENG, D.S., GAO, F.P. & LIANG, Z.D. 2019 Combined wave–current induced excess pore-pressure in a sandy seabed: flume observations and comparisons with theoretical models. *Coastal Engng* **147**, 89–98.

RAGIONE, L.L., LAURENT, K., JENKINS, J.T. & BEWLEY, G.P. 2019 Bedforms produced on a particle bed by vertical oscillations of a plate. *Phys. Rev. Lett.* **123**, 058501.

RAHMAN, M.M., LO, S.-C.R. & DAFALIAS, Y.F. 2014 Modelling the static liquefaction of sand with low-plasticity fines. *Géotecnique* **64**, 881–894.

REN, Y.P., XU, G.H., XU, X.B., ZHAO, T.L. & WANG, X.Z. 2020 The initial wave induced failure of silty seabed: liquefaction or shear failure. *Ocean Engng* **200**, 106990.

RIVERA-ROSARIO, G.A., DIAMESSIS, P.J. & JENKINS, J.T. 2017 Bed failure induced by internal solitary waves. *J. Geophys. Res.* **122**, 5468–5485.

RIVERA-ROSARIO, G.A., DIAMESSIS, P.J., LIEN, R.C., LAMB, K.G. & THOMSEN, G.N. 2020 Formation of recirculating cores in convectively breaking internal solitary waves of depression shoaling over gentle slopes in the South China Sea. *J. Phys. Oceanogr.* **50**, 1137–1157.

SUMER, B.M. 2014 Liquefaction around marine structures. In *Advanced Series on Ocean Engineering* (ed. P.L.-F. Liu). World Scientific.

SUMER, B.M. & FREDSØE, J. 2002 The mechanics of scour in the marine environment. In *Advanced Series on Ocean Engineering* (ed. P.L.-F. Liu). World Scientific.

SUMER, B.M., SEN, M.B., KARAGALI, I., CEREN, B., FREDSØE, J., SOTTILE, M., ZILIOLI, L. & FUHRMAN, D.R. 2011 Flow and sediment transport induced by a plunging solitary wave. *J. Geophys. Res.* **116**, C01008.

TEHRANIRAD, B., KIRBY, J.T. & SHI, F. 2020 A numerical model for tsunami-induced morphology change. *Pure Appl. Geophys.* **178**, 5031–5059.

TERZAGHI, K. 1943 *Theoretical Soil Mechanics*. John Wiley & Sons.
TONG, L.L., ZHANG, J.S., ZHAO, J.L., ZHENG, J.H. & GUO, Y.K. 2020 Modelling study of wave damping over a sandy and a silty bed. *Coastal Engng* **161**, 103756.
TØRUM, A. 2007 Wave-induced pore pressures-air/gas content. *ASCE J. Waterway Port Coastal Ocean Engng* **133**, 83–86.
ULKER, M.B.C. & RAHMAN, M.S. 2009 Response of saturated and nearly saturated porous media: different formulations and their applicability. *Intl J. Numer. Anal. Meth. Geomech.* **33**, 633–664.
VERRUIT, A. 1969 Elastic storage of aquifers. In *Flow through Porous Media* (ed. J.M. DeWiest). Academic Press.
WANG, Y.N. & YANG, D. 2019 Load-bearing analysis of the rock-socketed monopile in the shallow covering batholith seabed by finite element method. *Wind Power* **2**, 26–31.
WEN, J.G. & LIU, P.L.-F. 1995 Mass transport in water waves over an elastic bed. *Proc. R. Soc.* A **450**, 371–390.
YAMAMOTO, T. 1977 Wave-induced instability in sea beds. In *Proceedings of the ASCE Symposium on Coastal Sediments*, vol. 77, pp. 898–913. ASCE.
YAMAMOTO, T. 1978 Sea bed instability from waves. In *Proceedings of the Annual Offshore Technology Conference*, vol. 1, pp. 1819–1828. Offshore Technology Conference.
YAMAMOTO, T., KONING, H.K., SELLMEIJER, H. & HIJUM, E.V. 1978 On the response of a poro-elastic bed to water waves. *J. Fluid Mech.* **87**, 193–206.
YOUNG, Y.L., WHITE, J.A., XIAO, H. & BORJA, R.I. 2009 Liquefaction potential of coastal slopes induced by solitary waves. *Acta Geotech.* **4**, 17–34.
YOUNG, Y.L., XIAO, H. & MADDUX, T. 2010 Hydro- and morpho-dynamic modeling of breaking solitary waves over a fine sand beach. Part 1. Experimental study. *Mar. Geol.* **269**, 107–118.
ZEN, K. & YAMAZAKI, H. 1991 Field observation and analysis of wave-induced liquefaction in seabed. *Soils Found.* **31**, 161–179.
ZHAI, Y.Y., HE, R., ZHAO, J.L., ZHANG, J.S., JENG, D.S. & LI, L. 2018 Physical model of wave-induced seabed response around trenched pipeline in sandy seabed. *Appl. Ocean Res.* **75**, 37–52.
ZHAO, H.Y., ZHU, J.F., ZHENG, J.H. & ZHANG, J.S. 2020 Numerical modelling of the fluid-seabed-structure interactions considering the impact of principal stress axes rotations. *Soil Dyn. Earthq. Engng* **136**, 106242.